ORIGINAL RESEARCH

CD44-Receptors-Mediated Multiprong Targeting Strategy Against Breast Cancer and Tumor-Associated Macrophages: Design, Optimization, Characterization, and Cytologic Evaluation

Zahid Hussain [iD][1,2], Lama Abdulrahim Abdul Moti[1], Jayalakshmi Jagal[2], Hnin Ei Thu[3], Shahzeb Khan[4], Mohsin Kazi [iD][5]

[1]Department of Pharmaceutics and Pharmaceutical Technology, College of Pharmacy, University of Sharjah, Sharjah, 27272, United Arab Emirates; [2]Research Institute for Medical and Health Sciences, University of Sharjah, Sharjah, 27272, United Arab Emirates; [3]Department of Pharmacology, Faculty of Dentistry, Universiti Teknologi MARA, Sungai Buloh Campus, Sungai Buloh, Selangor, Malaysia; [4]Center for Pharmaceutical Engineering Science, Faculty of Life Sciences, School of Pharmacy and Medical Sciences, University of Bradford, West Yorkshire Bradford, BD7 1DP, UK; [5]Department of Pharmaceutics, College of Pharmacy, King Saud University, Riyadh, 11451 Saudi Arabia

Correspondence: Zahid Hussain, Department of Pharmaceutics and Pharmaceutical Technology, College of Pharmacy, University of Sharjah, Sharjah, 27272, United Arab Emirates, Email zhussain@sharjah.ac.ae

Introduction: Owing to its high prevalence, colossal potential of chemoresistance, metastasis, and relapse, breast cancer (BC) is the second leading cause of cancer-related fatalities in women. Several treatments (eg, chemotherapy, surgery, radiations, hormonal therapy, etc.) are conventionally prescribed for the treatment of BC; however, these are associated with serious systemic aftermaths. In this research, we aimed to design a multiprong targeting strategy for concurrent action against different phenotypes of BC (MCF-7 and SK-BR-3) and tumor-associated macrophages (TAMs) for relapse-free treatment of BC.

Methods: Paclitaxel (PTX) and tamoxifen (TMX) co-loaded chitosan (CS) nanoparticles (NPs) were prepared using the ionic-gelation method and optimized using the Design Expert® software by controlling different material attributes. For selective targeting through CD44-receptors that are heavily expressed on the BC cells and TAMs, the fabricated NPs (PTX-TMX-CS-NPs) were functionalized with hyaluronic acid (HA) as a targeting ligand.

Results: The optimized HA-PTX-TMX-CS-NPs exhibited desired physicochemical properties (PS ~230 nm, PDI 0.30, zeta potential ~21.5 mV), smooth spherical morphology, high encapsulation efficiency (PTX ~72% and TMX ~97%), good colloidal stability, and biphasic release kinetics. Moreover, the lowest cell viability depicted in MCF-7 (~25%), SK-BR-3 (~20%), and RAW 264.7 cells (~20%), induction of apoptosis, cell cycle arrest, enhanced cell internalization, and alleviation of MCF-7 and SK-BR-3 migration proved the superior anticancer potential of HA-PTX-TMX-CS-NPs compared to unfunctionalized NPs and other control medicines.

Conclusion: HA-functionalization of NPs is a promising multiprong strategy for CD44-receptors-mediated targeting of BC cells and TAMs to mitigate the progression, metastasis, and relapse in the BC.

Keywords: paclitaxel, tamoxifen, hyaluronic acid, polymeric nanoparticles, CD44-receptors, breast cancer, cell uptake, anticancer efficacy

Graphical Abstract
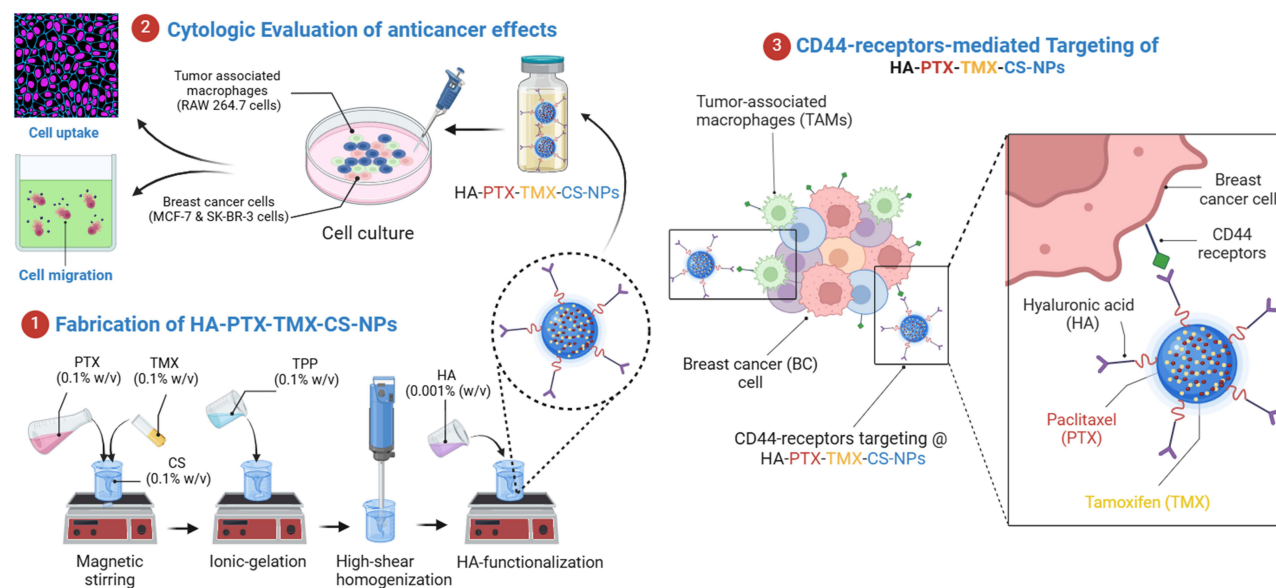
Introduction

Breast cancer (BC) is one of the most prevalent types of cancer and the second leading cause of cancer-related deaths in women globally, representing a significant health challenge with approximately 458,000 fatalities and more than a million new cases every year.[1] The International Agency for Research on Cancer (IARC) and the World Health Organization (WHO) reported that the incidences of BC are continuously escalating around the globe. The ineffectiveness of currently available conventional treatments and lack of early diagnosis are among the prime reasons for escalating rates and deaths in BC patients. Unfortunately, most BC patients are diagnosed at advanced stage (stage IV), where cancer has already metastasized to other tissues and organs of the body, and hence are difficult to treat. Common signs and symptoms of BC include, but not limited to, alteration in breast or nipple appearance, discharge from the nipples, presence of lump in the breast, skin dimpling, and persistent pain in the breast area or under the armpits.[2] BC patients who experience these signs and symptoms should undergo further investigations such as mammograms, ultrasound, magnetic resonance imaging (MRI), and tissue biopsies, to diagnose the stage of the BC.[3–5]

There are many approaches for the staging of BC; however, the TNM classification, which determines the stage of BC based on three important factors such as size and location of the tumor (T), involvement of lymph nodes (N), and the extent of metastasis (M). According to the TNM classification system, BC can be classified into four stages: stage I (early-stage) is characterized by tumor size of 2.0 cm or less. Based on metastasis, stage I can be further classified into stage IA, in which there is no involvement of surrounding lymph nodes, and stage IB which indicates the involvement of nearby lymph nodes. At stage II, the tumor size ranges between 2 and 5 cm with some metastasis to local tissues and may or may not involve the axillary lymph nodes. For example, stage IIA indicates no involvement of axillary lymph nodes and stage IIB indicates the spread of tumor to 1–3 axillary lymph nodes. At stage III, the tumor size is larger than 5.0 cm with moderate metastasis to the axillary or maxillary lymph nodes. Stage III can be subclassified into IIIA, IIIB, and IIIC. Stage IIIA identifies the spread of tumor to 4 to 9 lymph nodes or to the mammary lymph nodes but not to other parts of the body, or it indicates tumor size larger than 50 mm along with the involvement of 1–3 lymph nodes. On the other hand, stage IIIB indicates that the tumor has spread to the chest area or has caused breast to swell, or it is the inflammatory BC. In the stage IV (advanced stage), the tumor size is usually more than 5.0 cm with significant metastasis to the chest wall and other organs of the body (eg, liver, kidney, heart, brain, etc).

Tumor microenvironment (TME) play a crucial role in the progression, metastasis, and development of chemoresistance in BC. TME consists of extracellular matrix (ECM), stromal cells (eg, MSCs, fibroblasts, adipocytes, vasculature), red blood cells, pericytes, immune cells (eg, macrophages, natural killer cells, dendritic cells, and lymphocytes), cancer cells, and tumor-associated macrophages (TAMs).[6] TAMs are among the most abundant cells inhabiting the TME and play an important role in the development of TME via the dysregulation of various cytokines, chemokines, growth factors, angiogenesis, and immune function.[7] TAMs exhibit two polarized phenotypes of macrophages, M1 (antitumor) and M2 (protumor); however, the M2 phenotype is mainly exploited in the oncology research due to its abundance and dominance in the TME, especially when tumor grows and metastasizes to other tissues or organs of the body.[8] Moreover, the pro-oncogenic role of the M2-TAMs, such as promoting the angiogenesis, immune suppression, cancer cell proliferation and invasion, and development of chemoresistance, make them a key oncogenic target for alleviating the progression and growth of cancer.[7–10] Therefore, the M2-subtype of TAMs should be considered in addition to cancer cells while designing the new anti-neoplastic therapies for abolishing the chemoresistance, relapse, and cancer-related fatalities.

Depending upon the stage and the extent of metastasis, several treatment approaches are being clinically employed for the treatment of BC; however, the most prescribed treatments are chemotherapy, surgery, and radiotherapy. Surgery and radiotherapy are particularly beneficial for stage I and II BC, whereas stage III and IV BC patients usually require the chemotherapy. These treatment modalities can be used alone or in combination for more effective therapeutic outcomes. For example, the surgical resection of localized tumors can be followed by the chemotherapy to kill any remnants of BC cells/tissues. Chemotherapy can also be administered before surgery to shrink the tumor to minimize damage during the surgery. Chemotherapy and radiation can also be administered together to improve the therapeutic outcomes and mitigate chemoresistance and recurrence in cancer.[11] Despite the several advantages, conventional treatment modalities are associated with several adverse events that reduce their therapeutic significance and patient compliance.[12,13] To overcome these challenges, the safer, selective, targeted, and more efficacious treatments are urgently needed for the management of BC.[14–16]

Nanotechnology has emerged as a promising technology to mitigate most of the challenges associated with conventional treatments of BC.[17,18] Nanotechnology can be defined as the design, characterization, manipulation, and application of nanoscaled (1–1000 nm) materials. Like many other fields, the deployment of nanotechnology in chemotherapy has shown promising results in improving the therapeutic outcomes in BC treatment while mitigating the side effects associated with chemotherapy. Tumor targeting is one of the most investigated aspects of nanotechnology for the early detection and targeted treatment of different types of cancer.[19,20] There are different targeting mechanisms through which nanodelivery systems can target the TME in BC.[19–22] For example, the stimuli-responsive nanodelivery systems specifically respond to certain stimuli (eg, pH, enzymes, redox, ultrasound, magnetic, electric, light, etc.) to release their cargo into TME with minimal to no release in the systemic circulation or other body tissues.[19] Similarly, through several functionalization strategies (eg, PEGylation), the physicochemical properties of the nanodelivery systems can be enhanced to prolong their plasma half-life by impeding their early clearance from the body.[16,18] Conversely, an active targeting strategy refers to conjugation of high affinity targeting ligands (eg, hyaluronic acid, folic acid, transferrin, peptides, aptamers, etc.) on the surface of nanodelivery systems to specifically bind to some cell receptors (eg, CD44, folic acid, transferrin receptors, etc.) that are overexpressed on the surface of different cancer types.[23–25] The competitive binding of ligand-functionalized NPs to specific receptors on the cancer cells improves their internalization to the cancer cells, which enhances the cytotoxicity, apoptosis, and therapeutic efficacy of chemotherapeutics while mitigating their off-target effects.[26–29]

In this research, we have designed chitosan (CS)-NPs for the codelivery of paclitaxel (PTX) and tamoxifen (TMX) for synergistic action against the BC. For selective targeting of BC cells and TAMs through the CD44-receptors, the fabricated co-loaded NPs (PTX-TMX-CS-NPs) were functionalized with hyaluronic acid (HA) as a targeting ligand (Figure 1). The HA-functionalized NPs (HA-PTX-TMX-CS-NPs) were prepared using the ionic gelation method, optimized using the Design Expert® software, and characterized for various physicochemical properties such as particle size (PS), polydispersity index (PDI), zeta potential (ZP), encapsulation efficiency (EE%), morphology, colloidal stability, and in vitro release. The successful loading of PTX and TMX on CS-NPs and their functionalization with HA were confirmed using the Fourier transform infrared (FTIR) spectroscopy and differential scanning calorimetry (DSC). Moreover, the cell uptake efficiency,
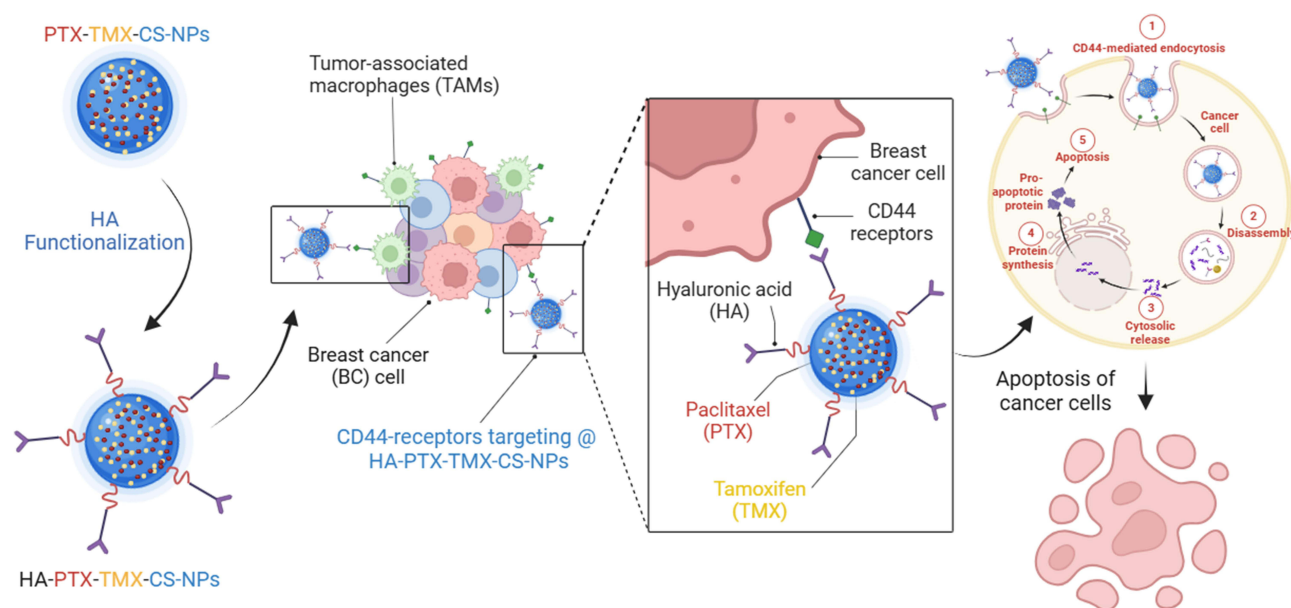
Figure 1 CD44-receptors-mediated targeting of HA-PTX-TMX-CS-NPs. Created in BioRender. Hussain, (**Z**) (2024) https://BioRender.com/r16v219.

cytotoxicity (IC_{50}), antiapoptotic effects, and the antimetastatic efficacy of HA-PTX-TMX-CS-NPs were assessed using two different phenotypes of BC cells (MCF-7 and SK-BR-3) and the M2-TAMs model (RAW 264.7 cells).

Materials and Methods
Materials
Low-molecular-weight chitosan (MW, 70 kDa; 85% deacetylated), pentasodium tripolyphosphate (TPP), tamoxifen (TMX), paclitaxel (PTX), hyaluronic acid (HA) (100 kDa), phosphate-buffered saline (PBS), and cellulose dialysis bags were purchased from Sigma–Aldrich, USA. MCF-7, SK-BR-3, RAW 264.7 cells, Dulbecco's modified Eagle's medium (DMEM), and Roswell Park Memorial Institute (RPMI) were purchased from AddexBio (San Diego, USA). Mounting media supplemented with DAPI, penicillin–streptomycin, coumarin-6, and MTT (3-(4,5-dimethylthiazol-2-YL)2,5-diphenyltetrazolium bromide) were purchased from Biomedical Scientific Services, Al Ain, UAE. All other chemicals were of analytical grade and were resourced from G40 laboratory and sister laboratories at Research Institute for Medical and Health Sciences (SIMHR), University of Sharjah, UAE.

Quality-by-Design (QbD) Approach for Optimization of PTX-TMX-CS-NPs
To design a new formulation or optimize an existing formulation, it is crucial to recognize critical material attributes (CMAs) and critical process parameters (CPPs) and to understand their effect on the critical quality attributes (CQAs) of the formulation. Therefore, we applied the D-optimal response surface design to optimize the HA-PTX-TMX-CS-NPs using the Design-Expert® software (version 13.0, Stat-Ease Inc., Minneapolis, MN, USA).

In our experimental design, two discrete numerical factors and one categorical factor were set as CMAs, and their effects on the chosen CQAs were investigated. The investigated CMAs were drug concentration (%w/v) (X_1), incubation time (min) (X_2), and homogenization (yes/no). The levels of independent variables were used to ensure a maximal design space as well as the reasonable processing of HA-PTX-TMX-CS-NPs (Table 1). To investigate the effect of studied CMAs (independent variables), five responses were evaluated such as, PS (Y_1), PDI (Y_2), ZP (Y_3), %EE of PTX (Y_4), and %EE of TMX (Y_5). To achieve the highest desirability value, the optimization goals were set for each response such as smallest PS, narrow PDI, highest ZP, highest %EE of PTX and TMX (Table 1).

Based on our experimental design, the Design-Expert® software generated 18 experimental runs including five replications (Table 2). All the experimental runs were conducted in triplicate (n = 3) in a random order to disregard the bias and to improve the predictability of the model. The responses were fitted to the linear and the quadratic response

Table 1 The Independent and Dependent Variables for the Optimization of PTX-TMX-CS-NPs

	Numerical Factor (discrete)	Applied Levels		
X_1	Drug concentration (% w/v)	0.01	0.05	0.1
X_2	Incubation time (min)	10	30	60
	Categorical Factor	**Applied Levels**		
X_3	Homogenization	Yes		No
	Responses	**Optimization Goal**		
Y_1	PS	Minimize		
Y_2	PDI	Minimize		
Y_3	ZP	Maximize		
Y_4	EE (%) PTX	Maximize		
Y_5	EE (%) TMX	Maximize		

Table 2 Experimental Design and Measured Responses for the Optimization of PTX-TMX-CS-NPs. X1: Drug Concentration (% w/v), X2: Incubation Time (Min), and X3: Homogenization (Yes/No)

Formulations	X_1 (%w/v)	X_2 (min)	X_3 (Yes/No)	Y_1 PS (nm)	Y_2 PDI	Y_3 ZP (mV)	Y_4 EE (%) PTX	Y_5 EE (%) TMX
F1	**0.05**	**60**	**No**	**190 ± 23**	**0.32 ± 0.03**	**27.3 ± 4.6**	**71.9 ± 5.2**	**96.6 ± 8.8**
F2	0.05	60	Yes	173 ± 13	0.30 ± 0.01	26.8 ± 5.2	68.9 ± 3.2	96.2 ± 7.9
F3	0.05	30	No	189 ± 18	0.34 ± 0.08	28.0 ± 3.5	69.2 ± 5.5	96.7 ± 5.6
F4	0.05	30	Yes	155 ± 16	0.31 ± 0.9	27.5 ± 3.8	67.7 ± 2.8	95.9 ± 9.2
F5	0.05	10	No	177 ± 22	0.31 ± 0.05	28.5 ± 2.7	66.7 ± 3.9	96.1 ± 9.6
F6	0.05	10	Yes	131 ± 13	0.28 ± 0.09	27.9 ± 4.2	66.1 ± 4.7	95.1 ± 7.2
F7	0.1	60	Yes	295 ± 11	0.44 ± 0.12	23.7 ± 3.5	71.4 ± 4.6	97.3 ± 5.9
F8	0.01	60	No	188 ± 14	0.35 ± 0.07	29.9 ± 5.9	62.6 ± 5.2	94.3 ± 9.1
F9	0.01	30	No	176 ± 9	0.35 ± 0.06	30.6 ± 4.2	61.2 ± 3.2	94.4 ± 8.6
F10	0.1	10	Yes	276 ± 12	0.43 ± 0.14	24.8 ± 2.2	65.9 ± 2.6	96.2 ± 6.9
F11	0.1	30	Yes	290 ± 21	0.45 ± 0.12	24.3 ± 3.7	68.5 ± 4.1	97.1 ± 9.3
F12	0.1	60	No	310 ± 22	0.47 ± 0.19	24.2 ± 2.1	74.0 ± 2.8	96.8 ± 8.4
F13	0.01	10	No	157 ± 14	0.32 ± 0.06	31.0 ± 4.8	59.5 ± 2.3	93.8 ± 4.9
F14	0.01	60	Yes	170 ± 17	0.34 ± 0.09	29.4 ± 5.1	59.4 ± 3.7	93.1 ± 5.6
F15	0.01	30	Yes	140 ± 13	0.33 ± 0.08	30.0 ± 5.9	59.3 ± 4.1	92.9 ± 10.2
F16	0.1	10	No	319 ± 23	0.47 ± 0.05	25.3 ± 2.2	66.2 ± 2.9	96.3 ± 9.5
F17	0.01	10	Yes	109 ± 8	0.30 ± 0.05	30.5 ± 3.8	58.6 ± 5.8	92.0 ± 7.5
F18	0.1	30	No	321 ± 12	0.49 ± 0.11	24.8 ± 2.9	69.8 ± 6.7	96.9 ± 9.2

surface models, and the resulting polynomial equations were statistically validated by the analysis of variance (ANOVA). To simplify the models, three and higher order interactions were neglected. Moreover, several statistical parameters, such as the p value, lack-of-fit p value, adjusted multiple correlation coefficient (adjusted R^2), predicted multiple correlation coefficient (predicted R^2), and multiple correlation coefficient (R^2), were determined. To enhance the significance of the model, the model with the maximum adjusted R^2 and predicted R^2 with an insignificant lack of fit was chosen.

Selection of Optimal Nanoformulation

After evaluating the significance of the chosen model for response prediction, 3D response surface plots were generated for each selected response to estimate the degree of interaction between different factors. The optimal value for each response was determined based on our optimization goals such as smallest PS, narrow PDI, highest ZP, and highest EE (%) of PTX and TMX. For the optimization, both numerical and graphical analyses were performed using the desirability function. Notably, the desirability values ranged between 0.0 and 1.0, and the value closest to 1.0 corresponds to desired response.[30,31]

Preparation of Blank (Drug-Free) CS-NPs

Prior to fabrication of drug-loaded CS-NPs, the blank CS-NPs were prepared using the ionic-gelation method in accordance with our previously established protocol[32,33] with minor modifications. Briefly, CS solution (0.1% w/v) was prepared by dissolving 100 mg of CS into 100 mL of acidified water (2% v/v acetic acid) using the magnetic stirrer for 3 h for complete homogenization and dissolution of CS. Similarly, 0.1% w/v TPP solution was prepared by dissolving 100 mg of TPP into 100 mL of distilled water using the magnetic stirrer for 5 min. Afterward, 10 mL of TPP solution was added dropwise into 25 mL CS solution while constantly stirring the mixture at 700 rpm for 30 min for the formation of blank CS-NPs.

Preparation of PTX-TMX Co-Loaded CS-NPs

According to our experimental design (Table 2), 18 different formulations (F1–F18) of PTX-TMX-CS-NPs were prepared using the ionic-gelation method.[32,33] Briefly, after preparation of CS solution (0.1% w/v) in the acidified water, the drug solutions (PTX and TMX) were incubated with CS solution to allow the maximum interaction of drugs with CS. To investigate the effect of drug concentration on the physicochemical properties of PTX-TMX-CS-NPs, different concentrations of drugs (0.01, 0.02, 0.03, 0.04, 0.05, 0.06, 0.07, 0.08, 0.09, and 0.1% w/v) were prepared from their stock solution (0.1% w/v). The stock solution was prepared by dissolving the 0.1 g of PTX and TMX into 100 mL of ethanol using the magnetic stirrer for 45 min at the room temperature. Moreover, the effect of incubation time (min) was evaluated by incubating the drug solution with CS solution for different time periods (10, 20, 30, 40, 50, and 60 min). At the end of each incubation period, 10 mL of TPP solution (0.1% v/v) was added dropwise into PTX-TMX-CS solution, resulting in the formation of PTX-TMX-CS-NPs. The fabricated PTX-TMX-CS-NPs dispersions were subjected to additional homogenization for 15 min to maximize the adsorption of drugs on to the surface of fabricated NPs. Finally, NPs dispersions were subjected to ultracentrifugation (Sorvall Evolution RC Superspeed Centrifuge, Thermo Fischer Scientific, USA) at 20,000 rpm for 30 min. The supernatants were collected to estimate the %EE and %LC, while NP pellets were harvested and redispersed into distilled water for further testing.

HA-Functionalization of Fabricated PTX-TMX-CS-NPs

For selective targeting of BC cells and TAMs through CD44 receptors, the fabricated PTX-TMX-CS-NPs were decorated with HA as a targeting ligand. For that, the fabricated PTX-TMX-CS-NPs were magnetically stirred (300 rpm) with 0.001% w/v HA solution for 3 h at the room temperature (23 ± 1°C). HA solution (0.001% w/v) was prepared by dissolving the 1.0 mg of HA into 100 mL of sodium acetate buffer (pH 5.5) using the magnetic stirrer at 1200 rpm for 30 min. The dispersions of HA-functionalized PTX-TMX-CS-NPs were finally subjected to ultracentrifugation (20,000 rpm) using the Optima L-100 XP Ultracentrifuge (Beckman-Coulter, USA) for 30 min at 10°C. The resulting NP pellets were harvested and redispersed into the distilled water for further testing.

Physicochemical Characterization

The mean PS (nm), ZP (mV), and PDI of the fabricated HA-PTX-TMX-CS-NPs were measured using the Malvern Nano-ZS Zetasizer (Malvern Instruments, UK) which principled at dynamic laser light scattering (DLS) technique. The physicochemical properties of HA-PTX-TMX-CS-NPs were compared with unfunctionalized drug-loaded NPs (PTX-TMX-CS-NPs).

Measurement of %EE of PTX and TMX

The %EE of PTX and TMX were measured using the Synergy H1 microplate reader (BioTek, USA). Briefly, the freshly prepared PTX-TMX-CS-NPs were subjected to ultracentrifugation (20,000 rpm for 30 min) using the Optima LE-80K Ultracentrifuge (Beckman-Coulter, USA) at 10°C. The %EE efficiency of PTX and TMX were estimated in the supernatant of NPs dispersions using the following equation:

Where, W_t indicates the initial amount of drugs and W_f refers to the amount of unloaded drugs in the supernatant. All the measurements were performed in triplicate (n=3), and the results are reported as mean ± SD.

Fourier Transform Infrared (FTIR) Spectrophotometric Analysis

FTIR analysis was performed to qualitatively validate the encapsulation of PTX and TMX into CS-NPs and their surface functionalization with HA. Briefly, 2 mg of lyophilized HA-PTX-TMX-CS-NPs was finely ground with potassium bromide (98 mg) using the mortar and pestle. Prior to grinding the material, the samples were placed in the oven overnight. The dried ground samples were then processed to make the scannable pellets using the hydraulic press, followed by scanning at 4000–400 cm^{-1}. The same procedure was used to scan CS, PTX, TMX, and unfunctionalized PTX-TMX-CS-NPs. The obtained FTIR spectra were interpreted based on characteristic peaks of different functional groups and characteristic shifts of various peaks, representing the specific structural and molecular changes in the materials.

Differential Scanning Calorimetric (DSC) Analysis

DSC is a powerful technique used to evaluate the thermal characteristics of test materials. DSC measures the heat flow into or out of a sample as a function of temperature or time, providing the meaningful information about the purity, phase transition, and thermal stability of the tested material. Briefly, the lyophilized powder of HA-PTX-TMX-CS-NPs was sealed in an aluminum-bottomed pan and subjected to thermal analysis using the Discovery DSC 25 instrument (Thermal Analyzer). A flow of nitrogen gas was introduced into the system to mitigate the oxidative and pyrolytic effects typically induced by the air. The temperature was increased from 20°C to 200°C at a constant rate of 10°C/min. For a comparative evaluation, the same protocol was followed to perform the DSC analysis for the raw material such as CS, TPP, PTX, TMX, and HA as well as the physical mixture of these ingredients. The DSC thermograms of HA-PTX-TMX-CS-NPs and the other materials were comparatively evaluated for their thermal characteristics, stability, purity, and compositional integrity.

Morphological Examination

The morphology of optimized HA-PTX-TMX-CS-NPs was analyzed using the scanning electron microscopy (SEM) (Zeiss Sigma 300 VP-FESEM). Briefly, NPs dispersion of HA-PTX-TMX-CS-NPs was subjected to ultracentrifugation (20000 rpm for 30 min) and the NPs pellet was collected, redispersed into the distilled water, and finally stored at –20°C. The frozen NPs dispersions were then subjected to lyophilization for 24 to 48 h. To minimize the dehydration effect of freeze-drying process, the optimized HA-PTX-TMX-CS-NPs were pretreated with mannitol as a lyoprotectant. The lyophilized NPs powder was redispersed into PBS (pH 7.4) by sonication for 5–10 min using the Branson 2510 ultrasonic cleaner (Marshall Scientific, USA). After complete redispersion, one drop of NPs dispersion was spread over a glass slide, carefully covered with a coverslip, and left to dry under vacuum. The test samples were then fixed on carbon tape, and a gold sputter module under high vacuum was used to sputter coat the dried NPs. Finally, the gold-coated NPs were scanned and imaged at an acceleration voltage of 3.0 kV using the SEM.

997

Storage Stability

One of the most significant challenges in the development of nanodelivery systems, particularly in the form of liquid dispersions, is their poor colloidal stability upon storage or after administration. Therefore, this experiment was conducted to evaluate the storage stability of our optimized HA-PTX-TMX-CS-NPs in the refrigerator (2–8°C) for a period of 8 weeks and results were compared with unfunctionalized PTX-TMX-CS-NPs. Briefly, the freshly prepared HA-PTX-TMX-CS-NPs dispersion was subjected to ultracentrifuge (20000 rpm for 30 min) and NPs pellets were redispersed into PBS (pH 7.4) with subsequent storage in the refrigerator. At various time points (day 1, week 1, 2, 3, 4, 5, 6, 7, and week 8), 2 mL of the samples were withdrawn and analyzed for the mean PS (nm), PDI, and ZP (mV) using the Malvern Nano-ZS Zetasizer (Malvern Instruments, UK).

In-vitro Release

To estimate the release kinetics of PTX and TMX from the optimized HA-PTX-TMX-CS-NPs, we performed the in vitro release experiment. Moreover, the effect of pH on the release pattern of both encapsulated drugs was also analyzed. Briefly, the freshly prepared lyophilized HA-PTX-TMX-CS-NPs were redispersed into 10 mL of PBS (pH 6.0 and 7.4) and introduced into dialysis tubes, which were then tide up from both ends. The dialysis tubes were then immersed into 10 mL of dissolution media (PBS/ethanol, 50:50 @ pH 6.0 and 7.4) and placed in water bath at 37°C while constantly stirring at 200 rpm. At various time points, 1.0 mL of the dialysate was withdrawn and replenished with the same volume of the fresh media. The standard calibration curves were generated and used to calculate the cumulative release of both drugs. The amount of drug released was measured using the UV–visible spectroscopy.[33,34]

Cytologic Evaluation

A series of in vitro experiments were conducted using two different phenotypes of BC cells (MCF-7 and SK-BR-3) and M2-TAMs model (RAW 264.7) to evaluate the cytotoxicity, IC_{50}, cell cycle arrest, apoptotic potential, cellular uptake efficiency, and antimetastatic efficacy of optimized HA-PTX-TMX-CS-NPs, and results were compared with unfunctionalized PTX-TMX-CS-NPs, native drugs (PTX+TMX), blank CS-NPs, and control (untreated) groups. Prior to conduct the cell culture experiments, MCF-7 and SK-BR-3 cells were cultured in Roswell Park Memorial Institute (RPMI-1640) media supplemented with 10% fetal bovine serum (FBS) and 1% streptomycin/penicillin. On the other hand, RAW 264.7 cells were cultured in Dulbecco's modified Eagle's medium (DMEM) supplemented with 10% FBS and 1% streptomycin/penicillin. The cultured cells were incubated at 37°C in the incubator with a humidified atmosphere containing 5% CO_2.

Cytotoxicity and IC_{50}

To evaluate the cytotoxic potential of optimized HA-PTX-TMX-CS-NPs against BC cells and TAMs in comparison with unfunctionalized PTX-TMX-CS-NPs, blank CS-NPs, HA-CS-NPs, free drugs (PTX+TMX), and control (untreated), we conducted the MTT (3-(4,5-dimethylthiazol-2-yl)-2,5-diphenyltetrazolium bromide) assay. Briefly, 5×10^3 cells were seeded into each well of 96-well plate and treated with different concentrations of NPs or remained untreated. After 24 h, 10 μL of 5 mg/mL MTT solution was added to each well, and 96-well plate was incubated at 37°C for 4 h. At the end of the incubation period, cell culture media was removed from each well, 100 μL of DMSO was added to dissolve formazan crystals, and the optical density (OD) of each well was measured at 570 nm using the Synergy H1 (BioTek) ultraviolet spectrophotometer. The percentage of viable cells was calculated using the following equation:

We further evaluated the cytotoxic potency of our optimized HA-PTX-TMX-CS-NPs by estimating its IC_{50} value (half-maximal inhibitory concentration), in comparison with unfunctionalized PTX-TMX-CS-NPs and free drugs (PTX+TMX). The obtained results are reported as mean (n = 3) ± S.D. Moreover, the cell morphology of treated cells was assessed using the light microscopy (magnification 20×, scale bar = 100 μm) to evaluate the apparent cellular damage or morphological changes (eg, shrinkage, cell membrane disruption, apoptotic bodies, etc.) observed in BC cells (MCF-7 and SK-BR-3) and TAMs (RAW 264.7) followed by treatment with different formulations.

Cell Apoptosis

This experiment was performed to detect early- or late-stage apoptosis or necrotic potential of our optimized HA-PTX-TMX-CS-NPs using the MCF-7, SK-BR-3, and RAW 264.7, and results were compared with unfunctionalized PTX-TMX-CS-NPs, free drugs (PTX+TMX), blank CS-NPs, and control (untreated) groups. This experiment was performed using the Annexin V-FITC and the viability dye 7-AAD Apoptosis Detection Kit according to the manufacturer's instructions. Briefly, 7.5×10^4 cells were plated into 60 mm petri dishes and incubated at 37°C for 24 h in DMEM. The cells were then treated with 10 μg/mL of HA-PTX-TMX-CS-NPs for 24 h, washed three times with PBS (pH 7.4) and resuspended in the binding buffer (10 mm HEPES/NaOH, pH 7.4, 140 mm NaCl, 2.5 mm CaCl$_2$). Afterward, Annexin V-FITC conjugate (250 ng) and 7-AAD dye solution (1 μg) were added to each cell suspension (500 μL), followed by incubation at the room temperature for 10 min in the dark. Finally, the cells were analyzed using the flow cytometer (BD Biosciences, San Jose, CA, USA). The obtained results were compared with unfunctionalized PTX-TMX-CS-NPs, free drugs (PTX+TMX), blank CS-NPs, and control (untreated) groups.

Cell Cycle

To analyze the relative proportions of MCF-7, SK-BR-3, and RAW 264.7 cells into different phases (G1, S, G2, M) of the cell cycle, the cell cycle analysis was performed using the flow cytometer (BD Biosciences, San Jose, CA, USA). Briefly, 8.5×10^4 cells/mL were seeded into 60 mm petri dishes and incubated for 24 h followed by treatment with HA-PTX-TMX-CS-NPs (10 μg/mL) for 24 h. The cells were then harvested with trypsin/EDTA solution, washed in PBS, fixed with 70% ethanol (ice-cold) and kept at –20°C. The fixed cells were then centrifuged, resuspended into DNA extraction buffer (0.2 M Na$_2$PO$_4$ and 0.1 M citric acid, pH 7.8), and incubated at 37°C for 30 min. Finally, cells were incubated with a dye solution (0.1% Triton X-100 + 20 μg/mL PI + 200 μg/mL RNAse + PBS) for 1 h in the dark, followed by analysis using the flow cytometer. The obtained results were compared with unfunctionalized PTX-TMX-CS-NPs, free drugs (PTX+TMX), blank CS-NPs, and control (untreated) groups.

Cell Uptake

This experiment was performed to evaluate the cell internalization efficiency of our optimized HA-functionalized NPs into MCF-7, SK-BR-3, and RAW 264.7 cells using the confocal laser scanning microscopy (CLSM) (Nikon Eclipse Ti, Melville, New York, USA). In this experiment, we used coumarin (CMR) as a fluorescent dye (which acquires bright green color under fluorescent microscope) to analyze the cell uptake efficiency of different test groups. Notably, HA-functionalized CMR-CS-NPs (HA-CMR-CS-NPs) and unfunctionalized CMR-CS-NPs were prepared using the same protocol (Preparation of PTX-TMX Co-Loaded CS-NPs and 2.6), adapted for the HA-PTX-TMX-CS-NPs and unfunctionalized PTX-TMX-CS-NPs. Briefly, 1×10^3 cells were plated into each well of 6-well plate, covered with coverslip, and incubated at 37°C for 24 h to allow cell adhesion. At the end of the incubation period, cells were treated with HA-CMR-CS-NPs and incubated for 24 h at 37°C. The same treatment protocol was used for other test formulations such as unfunctionalized CMR-CS-NPs, free CMR, and control (untreated) groups. After 24 h, cells were washed thrice with PBS (pH 7.4) and fixed with 5% paraformaldehyde (PFA) solution for 30 min. After that, cells were washed again with PBS (pH 7.4) twice, and their nuclei were stained with DAPI (containing mounting solution) for 20 min at the room temperature. Finally, the fluorescence images of treated cells were taken (60× magnification) using the CLSM with violet (405 nm) and blue (488 nm) lasers.

Taken together, the cell uptake efficiency of HA-CMR-CS-NPs into MCF-7, SK-BR-3, and RAW 264.7 was also assessed using the flow cytometry (BD Biosciences, San Jose, CA, USA), and results were compared with unfunctionalized CMR-CS-NPs, free CMR, and control groups. Briefly, 1×10^3 cells were plated into each well of 6-well plate, covered with coverslip, and incubated at 37°C for 24 h to allow cell adherence. After 24 h of incubation, cells were treated with HA-CMR-CS-NPs and incubated for another 24 h at 37°C. At the end of the incubation period, cells were harvested via trypsinization and washed thrice with PBS (pH 7.4). The collected cells were then analyzed to detect the fluorescence intensity using the BD FACSAria™ III Flow Cytometer. The standard fluidics, optical, and electronic configurations were used to acquire the resulting data using the BD FACSDiva software with subsequent analysis by FlowJo software (FlowJo LLC., Ashland, Oregon, USA).

Scratch Assay

Cancer cell migration play an important role in the progression, invasion, and metastasis of BC. Therefore, we conducted the scratch assay to evaluate the anti-metastatic potential of optimized HA-PTX-TMX-CS-NPs in comparison with unfunctionalized PTX-TMX-CS-NPs, free drugs (PTX+TMX), blank HA-CS-NPs, and control groups using the MCF-7 and SK-BR-3 cells. Briefly, 1×10^5 cells were seeded into each well of 24-well plate and incubated for 24 h at 37°C to allow cells adherence to form a confluent cell monolayer. After 24 h of incubation, a scratch was introduced into each cell monolayer using a 1.0 mm pipette tip. The scratched cell monolayers were then treated with 100 μg/mL of HA-PTX-TMX-CS-NPs, PTX-TMX-CS-NPs, free drugs (PTX+TMX), blank HA-CS-NPs, or remained untreated (control). Finally, the microscopy images of all scratched cell monolayers were captured (4× magnification, scale bar = 150 μm) at different time points (0 h, 24 h, and 48 h) using the light microscope (IM-3 OPTIKA).

Statistical Analysis

All experiments were performed in triplicates (n = 3) and the resulting data were reported as mean ± S.D. The statistical analysis of the obtained results was carried out using the Prism version 9 (GraphPad Software, USA). Student's t test was applied for comparing two test groups, while one-way analysis of variance (ANOVA) was utilized for the analyses involving the multiple comparisons.

Results and Discussion

QbD Approach for Optimization of PTX-TMX-CS-NPs

To produce the PTX-TMX-CS-NPs with optimum physicochemical properties (ie, PS, PDI, ZP, and %EE), QbD approach (Design Expert® software) was applied to investigate the effect of different CPPs and CMAs on the chosen CQAs of fabricated NPs.[31] The D-optimal response surface design demonstrated a significant effect of investigated factors such as drug concentration (X_1), incubation time (X_2), and homogenization (X_3) on various CQAs of the fabricated PTX-TMX-CS-NPs (Figure 2). The mean PS of PTX-TMX-CS-NPs was varied from 109 ± 8 nm to 321 ± 12 nm, PDI was varied from 0.30 ± 0.01 to 0.49 ± 0.11, ZP was varied from 23.7 ± 3.5 mV to 31.0 ± 4.8 mV, %EE of PTX ranged from 58.6 ± 5.8% to 74.0 ± 2.8%, and %EE of TMX was varied from 92.0 ± 7.5% to 97.3 ± 5.9%. For each response (eg, PS, PDI, ZP, and %EE of PTX and TMX), a mathematical expression in the form of second-order polynomial equation was generated from the statistical analysis of our experimental design. These mathematical expressions have reported the intercept and regression co-efficient of studied factors (X_1-X_3), as described below:
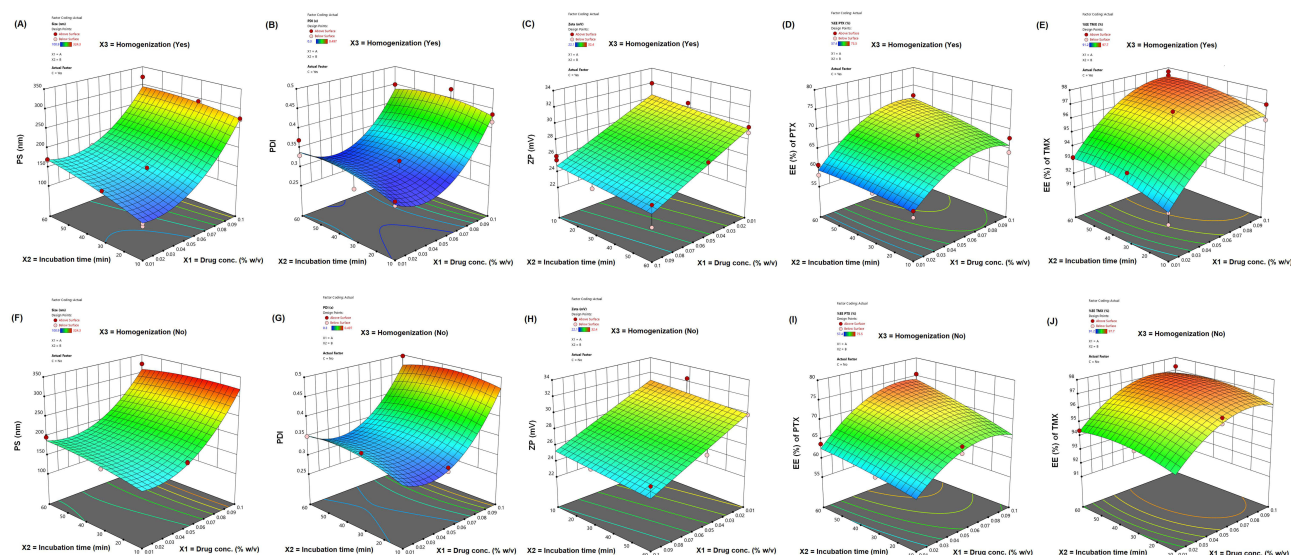

Figure 2 Response surface plots for the effects of drug concentration (X_1), incubation time (X_2), and homogenization (X_3) on the mean PS (Y_1) (**A** and **F**), PDI (Y_2) (B and **G**), ZP (Y_3) (C and **H**), and %EE of PTX (Y_4) (D and **I**) and TMX (Y_5) (E and **J**).

$$\textbf{PS} = 182.04 + 71.96X_1 + 12.76X_2 + 15.54X_3 - 10.35X_1X_2 - 0.9221X_1X_3 - 7.26X_2X_3 + 52.65X_1{}^2 - 6.88X_2{}^2$$

$$\textbf{PDI} = 0.3315 + 0.0622X_1 + 0.0091X_2 + 0.0134X_3 - 0.0078X_1X_2 + 0.0055X_1X_3 - 0.0014X_2X_3 + 0.0770X_1{}^2 - 0.0176\times_2{}^2$$

$$\textbf{ZP} = 27.33 - 2.85X_1 - 0.5494X_2 + 0.2657X_3$$

$$\textbf{EE}_{\textbf{PTX}}(\%) = 69.45 + 4.69X_1 + 2.16X_2 + 0.8749X_3 + 1.18X_1X_2 - 0.1414X_1X_3 + 0.5743X_2X_3 - 4.29X_1{}^2 - 0.4509X_2{}^2$$

$$\textbf{EE}_{\textbf{TMX}}(\%) = 96.67 + 1.66X_1 + 0.4090X_2 + 0.3183X_3 + 0.0064X_1X_2 - 0.4337X_1X_3 - 0.1501X_2X_3 - 1.24X_1{}^2 - 0.4450X_2{}^2$$

For each response (eg, PS, PDI, ZP, and %EE of PTX and TMX), a model with highest possible predicted R^2 and adjusted R^2 and with equitable agreement between both parameters was chosen (Table 3). In accordance with the lack of fit analysis (*p value*), the quadratic model was best fit to analyze the effect of investigated factors (X_1, X_2, X_3) on the PS, PDI, and %EE of PTX and TMX, while the linear model was best fit to analyze their effects on ZP (Figure 2).

Effect of Drug Concentration

The obtained 3D response surface plots indicated that drug concentration (X_1) exhibited a significant ($p<0.0001$) impact on the mean PS of fabricated PTX-TMX-CS-NPs (Table 3). A consistent increase in the mean PS of PTX-TMX-CS-NPs from 109 ± 8 nm to 321 ± 12 nm was observed when drug concentration (PTX+TMX) was increased from 0.01 to 0.1% (w/v), and the smallest PS (109 ± 8 nm) was obtained at 0.01% (w/v) drug concentration (Figure 2). The increase in the mean PS of PTX-TMX-CS-NPs was likely due to differences in the degree and extent of crosslinking of amino groups ($-NH_3{}^+$) of CS and ($-PO_4{}^-$) of TPP at different concentrations of drugs, which ultimately affects the kinetics of NPs formation during the ionic-gelation process. A possible increase in the viscosity of polymeric solution due to increasing concentrations of drugs could be another argument that explains the resulting increase in the mean PS of fabricated PTX-TMX-CS-NPs due to changes in nucleation and growth processes.[35,36]

Another important property of NPs is the PDI, which indicates the uniformity of size distribution and colloidal stability of NPs formulation. A lower PDI (closer to zero) indicates greater stability of NPs due to lower propensity of Ostwald ripening when exposed to fluctuating temperature. Conversely, a higher PDI indicates less stability due to greater likelihood of Ostwald ripening under similar conditions.[32,33] Our resulting data showed that drug concentration (X_1) had a significant ($p<0.0001$) effect on the PDI (Y_2) of fabricated PTX-TMX-CS-NPs (Table 3). In general, higher

Table 3 Outcomes of the Experimental Design

Response	Model	R^2	Adjusted R^2	Predicted R^2	Lack of fit p value	Model p value	Most significant terms
PS (nm)	Quadratic	0.9706	0.9470	0.8803	0.7275	<0.0001	X_1 (p<0.0001) X_2 (p=0.0226) X_3 (p=0.0039) $X_1{}^2$ (p=0.0003)
PDI	Quadratic	0.9251	0.8652	0.7101	0.2384	0.0001	X_1 (p<0.0001) $X_1{}^2$ (p=0.0004)
ZP (mV)	Linear	0.8378	0.8053	0.7427	0.4635	<0.0001	X_1 (p<0.0001)
%EE$_{PTX}$	Quadratic	0.9400	0.8921	0.7503	0.4701	<0.0001	X_1 (p<0.0001) X_2 (p=0.0015) $X_1{}^2$ (p=0.00118)
%EE$_{TMX}$	Quadratic	0.9216	0.8590	0.7218	0.0808	0.0001	X_1 (p <0.0001) $X_1{}^2$ (p = 0.0153)

PDIs were observed at higher drug concentrations, and the lowest PDI (0.28 ± 0.09) was evident at 0.05% (w/v) drug concentration (Figure 2).

ZP is also a crucial physicochemical feature of NPs that can affect their colloidal stability by reducing their agglomeration potential. ZP also affects the membrane permeability, cellular uptake, pharmacokinetics, tissue biodistribution, clearance, and the therapeutic efficacy of NPs.[37,38] Our results revealed that drug concentration (X_1) exhibits a significant ($p<0.0001$) effect on the ZP (Y_3) of fabricated PTX-TMX-CS-NPs (Table 3). A consistent decrease in the ZP of NPs was observed when drug concentration was increased from 0.01% to 0.1% (w/v), and the highest ZP (+31.0 ± 4.8 mV) was observed at 0.01% (w/v) drug concentration (Figure 2). The decrease in the ZP of NPs at increasing drug concentration could be due to the interaction of drugs with the cationic surface of NPs. PTX, which is a negatively charged compound at the acidic pH, could possibly interact with positively charged CS ($-NH_3^+$), leading to shielding of cationic charges of CS and ultimately reduction in the ZP of CS-NPs.[39]

%EE is a promising characteristic of a nanodelivery system, determining its pharmacokinetics, effectiveness, therapeutic efficacy, and the safety. Our results demonstrated that drug concentration (X_1) had a significant ($p<0.0001$) effect on the %EE of PTX (Y_4) and TMX (Y_5) in the PTX-TMX-CS-NPs (Table 3). It was evident that %EE of PTX and TMX were increased from 58.6 ± 5.8% to 74.0 ± 2.8% and from 92.0 ± 7.5% to 97.3 ± 5.9%, respectively, when drug concentration was increased from 0.01 to 0.1% (w/v) (Figure 2). This can be explained by this fact that higher drug concentration might result in better interaction with CS matrix, leading to more efficient encapsulation and adsorption. At higher concentration, drug molecules might interact more effectively with the available binding sites on the polymeric chain of CS, leading to higher entrapment and adsorption on to fabricated PTX-TMX-CS-NPs.[33]

Effect of Incubation Time

The effect of drug incubation time on the mean PS of NPs is complex and depends on several factors including, drug-nanomaterial interactions. To determine the optimum incubation time for NPs, the experimental characterization and optimization are crucial. Our results indicated that the mean PS (Y_1) of PTX-TMX-CS-NPs was significantly ($p<0.022$) varied between 109 ± 8 nm to 321 ± 12 nm when drug incubation time (X_2) was varied between 10 and 60 min, which could be due to enhanced encapsulation and adsorption of drugs on CS-NPs.[40,41] Another possible reason could be the temporary agglomeration of NPs upon prolonged exposure to drugs. On the other hand, the effect of incubation time on PDI (Y_2), ZP (Y_3), and %EE of TMX (Y_5) was not significant; however, a significant effect ($p<0.0015$) of incubation time was evident on %EE of PTX (Y_4) (Table 3). This could be due to greater hydrophobicity of PTX compared to TMX, which might require relatively longer incubation time with NPs to undergo electrostatic and/or hydrophobic interactions, leading to greater adsorption of PTX on the CS-NPs.[40,41]

Effect of Homogenization

Following the preparation of PTX-TMX-CS-NPs, we employed an additional homogenization step (15 min), aiming to maximize drug adsorption on the surface of NPs, de-aggregation of NPs, and to improve the uniformity of size distribution. Our results revealed that additional homogenization (X_3) exhibited a significant effect ($p<0.0039$) on the mean PS (Y_1) of PTX-TMX-CS-NPs, but an insignificant effect on the PDI (Y_2), ZP (Y_3), and %EE of PTX (Y_4) and TMX (Y_5) (Table 3). These findings indicated that an additional homogenization step could influence only the mean PS without affecting the other physicochemical properties of PTX-TMX-CS-NPs; therefore, we anticipated that additional homogenization step is not mandatory to produce the NPs with desired physicochemical features.

Selection of Optimal Nanoformulation

In accordance with our optimization results (Table 3), the PTX-TMX-CS-NPs prepared with 0.5 mg/mL drug concentration, incubated for 60 min, and without homogenization exhibited the most desirable physicochemical properties. With a maximum desirability of 0.792, the optimized PTX-TMX-CS-NPs showed the highest level of optimization for all CQAs such as the mean PS (Y_1) of 190 ± 23 nm, PDI (Y_2) of 0.32 ± 0.03, ZP (Y_3) of 27.3 ± 4.6 mV), %EE of PTX (Y_4) of 71.9 ± 5.2%, and %EE of TMX (Y_5) of 96.6 ± 8.8 (Figure 3).

The physicochemical properties of NPs play a crucial role in their colloidal stability, release kinetics, cellular uptake, cytotoxicity, pharmacokinetics, tumor targeting, and anticancer efficacy. Specifically, PS (<200 nm), narrow PDI, high
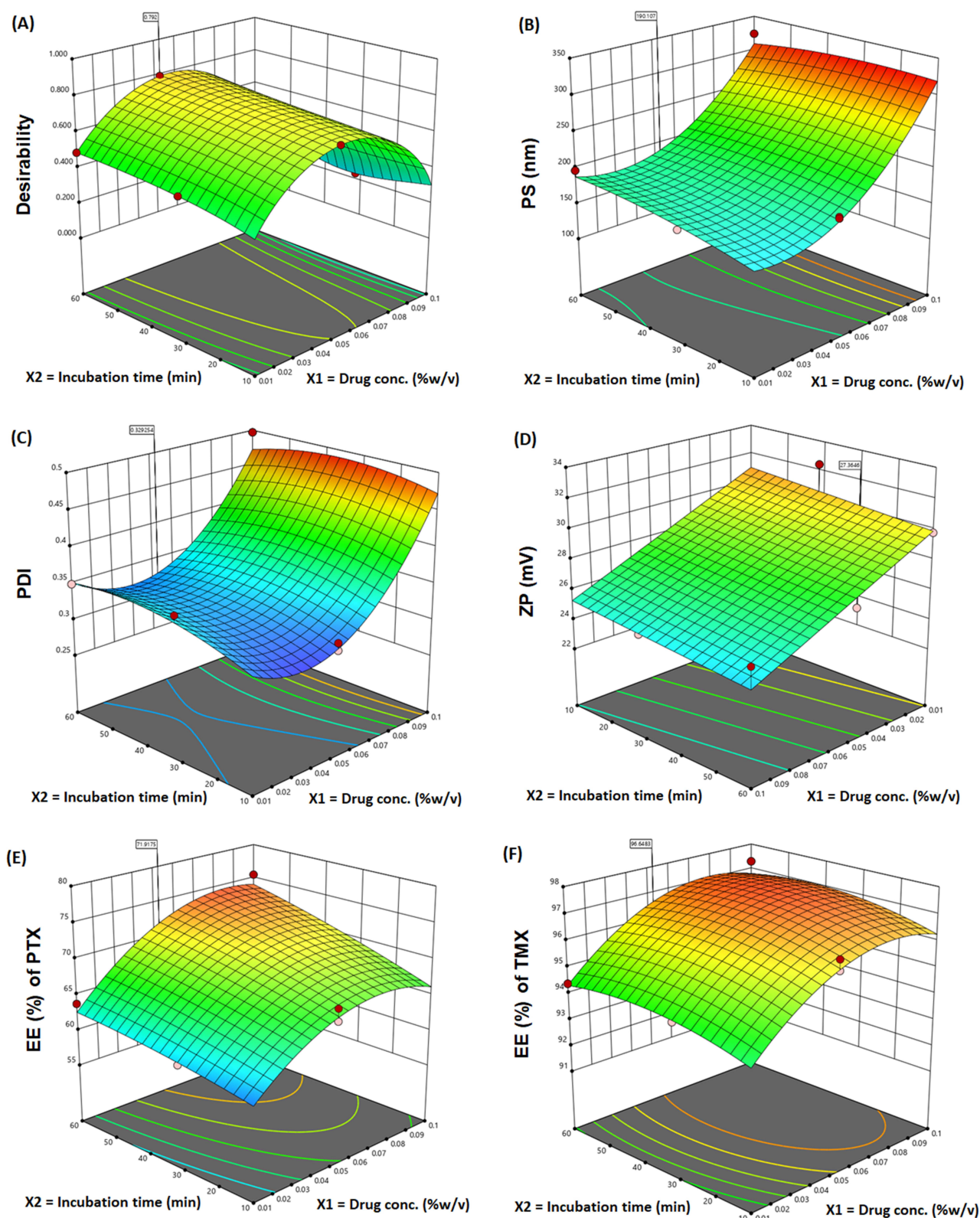
Figure 3 Response surface plots for the desirability value (**A**) and the optimum levels of the studied CQAs such as mean PS (**B**), PDI (**C**), ZP (**D**), and %EE of PTX (**E**) and TMX (**F**) of the optimized PTX-TMX-CS-NPs based on the investigated factors (X_1, X_2, X_3).

ZP (>±30 mV), high %EE, spherical morphology, and sustained release are highly desirable features of NPs for passive tumor targeting. These NPs can easily navigate through the underdeveloped blood capillaries and leaky tumor endothelium and can retain in the TME for an extended period due to minimal lymphatic drainage to exert a powerful anticancer effect.

HA-Functionalized PTX-TMX-CS-NPs

The optimized PTX-TMX-CS-NPs were further decorated with HA (0.001% w/v) for the selective targeting of BC cells and TAMs through CD44 receptors. The resulting HA-PTX-TMX-CS-NPs exhibited nanoscaled dimension (PS = 230 ± 21 nm), narrow PDI (0.30 ± 0.04), good ZP (21.5 ± 3.4 mV), and high %EE of PTX 71.9 ± 5.2% and TMX 96.6 ± 8.8.

FTIR Analysis

The successful encapsulation of PTX and TMX into CS-NPs and functionalization with HA were qualitatively assessed using the FTIR analysis (Figure 4). The characteristic peaks appeared in the FTIR spectra of native CS included
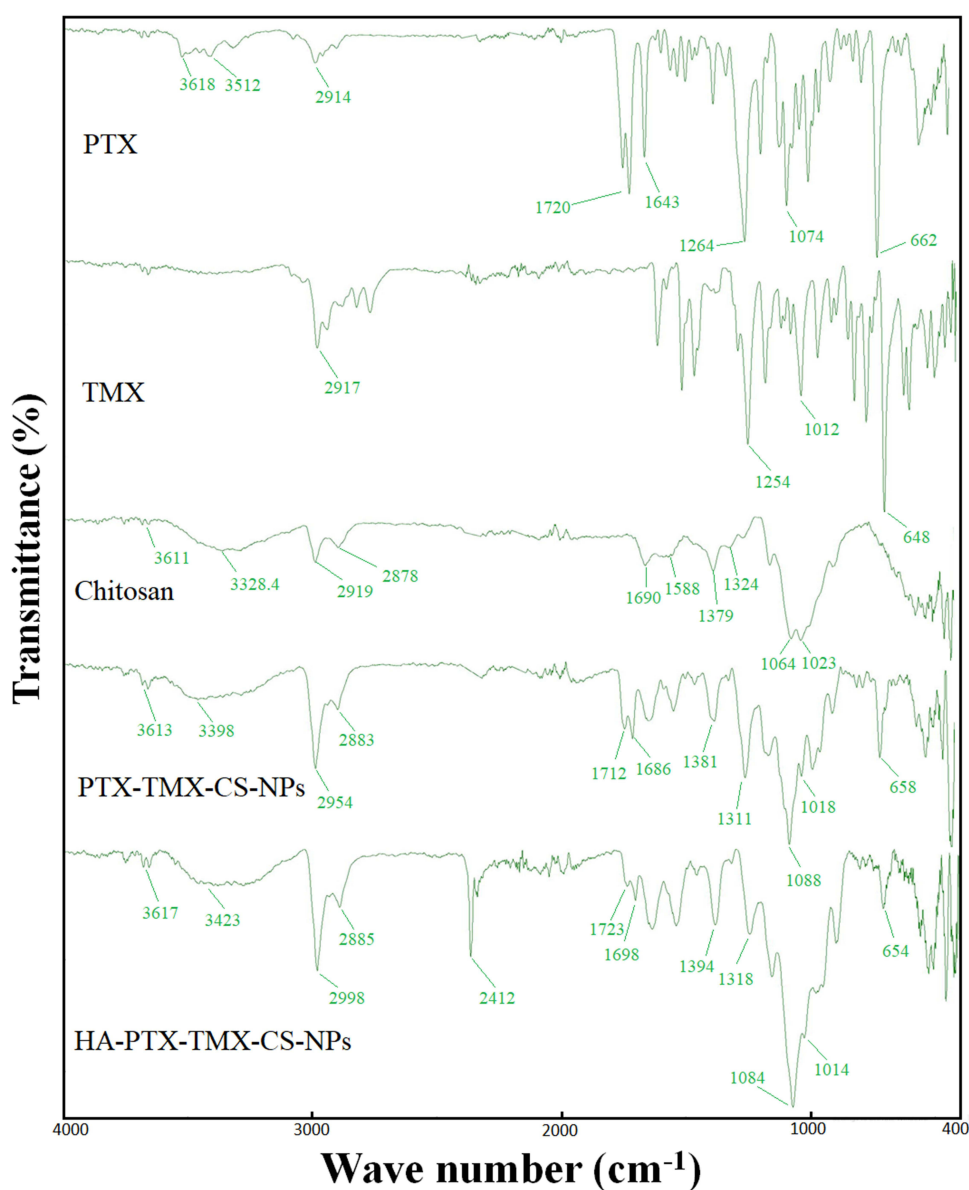
Figure 4 FTIR analysis of HA-PTX-TMX-CS-NPs in comparison with PTX-TMX-CS-NPs and the raw material such as pure PTX, TMX, and CS.

3611 cm^{-1} and 3328.4 cm^{-1} (OH stretching, alcoholic), 2919 cm^{-1} and 2878 cm^{-1} (C–H stretching), 1690 cm^{-1} (N–H stretching in amide I), 1588 cm^{-1} (N–H bending in $–NH_2$), 1379 cm^{-1} (C–H bending in $–CH_2$), 1324 cm^{-1} (C–N vibration in amide III), and 1064 cm^{-1} and 1023 cm^{-1} (C–O stretching).[32,33] FTIR spectrum of PTX displayed characteristic peaks at 3618 cm^{-1} (–OH stretching), 2914 cm^{-1} (C–H stretching), 1720 cm^{-1} (C=O stretching), 1643 cm^{-1} (C=C stretching), 1264 cm^{-1} and 1074 cm^{-1} (C–O stretching), and 662 cm^{-1} (C=C bending). TMX spectra displayed characteristic peaks at 2917 cm^{-1} (C–H stretching), 1254 cm^{-1} and 1012 cm^{-1} (C–N stretching), and 648 cm^{-1} (C=C bending). The data interpretation revealed that the peak of –OH stretching (3328.4 cm^{-1}) in the spectra of pure CS was shifted to 3398 cm^{-1} and 3423 cm^{-1} in the spectra of PTX-TMX-CS-NPs and HA-PTX-TMS-CS-NPs, respectively (Figure 4). Moreover, the absorption band at 3611 cm^{-1} in the plain CS spectra became sharper and more intense in the spectra of PTX-TMX-CS-NPs and HA-PTX-TMX-CS-NPs, which indicates an enhanced hydrogen bonding. On the other hand, the characteristic peaks of C-H stretching, which appeared at 2919 cm^{-1} and 2878 cm^{-1} in the spectrum of plain CS, were shifted to 2954 cm^{-1} and 2883 cm^{-1} in the spectra of PTX-TMX-CS-NPs and to 2998 cm^{-1} and 2885 cm^{-1} in the spectra of HA-PTX-TMX-CS-NPs, respectively (Figure 4). These shifts indicate interactions between CS, PTX, TMX, and HA. Other conformational changes including the shifting of 1690 cm^{-1} and 1588 cm^{-1} peaks in the plain CS spectra to 1712 cm^{-1} and 1686 cm^{-1} in the spectra of PTX-TMX-CS-NPs and to 1723 cm^{-1} and 1698 cm^{-1} in the spectra of HA-PTX-TMX-CS-NPs, also indicate interactions between $–NH_3^+$ groups of CS, PTX, TMX, and HA. Moreover, an obvious decrease in the intensity of absorption band at 1690 cm^{-1} was observed in the spectra of PTX-TMX-CS-NPs and HA-PTX-TMX-CS-NPs compared to plain CS also indicates interactions between these ingredients. The characteristic peaks at 1379 cm^{-1} and 1324 cm^{-1} in the plain CS spectra also shifted to 1381 cm^{-1} and 1311 cm^{-1} in the spectra of PTX-TMX-CS-NPs and to 1394 cm^{-1} and 1318 cm^{-1} in the spectra of HA-PTX-TMX-CS-NPs.[32,33] Two additional sharp absorption bands of good intensity were noted in the spectra of HA-PTX-TMX-CS-NPs at 2412 cm^{-1} and 654 cm^{-1}, which also indicated the successful loading of PTX and TMX and functionalization with HA (Figure 4).

DSC Analysis

The encapsulation of PTX and TMX into CS-NP and their functionalization with HA were also validated by analyzing the thermal behavior of HA-PTX-TMX-CS-NPs in comparison with the raw material using the DSC analysis (Figure 5). The obtained DSC thermogram of CS showed a broad peak appeared at 82.75°C (enthalpy 34.749 J/g with onset at 38.34°C), which indicates an endothermic reaction that could be due to melting, polymorphic conversion, or denaturation of CS. A sharp peak at 104.8°C (enthalpy of 65.873 J/g with an onset at 95.88°C) in the DSC thermogram of PTX indicated an endothermic reaction, which could be due to melting, polymorphic conversion, or denaturation of PTX. The melting point of PTX was noted to be 226.93°C. In the DSC thermogram of TMX, a sharp peak at 82.75°C (enthalpy of 89.95 J/g with an onset at 95.88°C) indicated an endothermic reaction, which could be due to melting, polymorphic conversion, or denaturation of TMX. The melting point of TMX was 95.9°C. On the other hand, a sharp peak at 116.79°C (enthalpy 86.258 J/g with onset at 114.91°C) indicated an endothermic reaction, which could be due to melting, polymorphic conversion, or denaturation of TPP. The melting point of TPP was 115.0°C. In the DSC thermogram of HA, a broad peak at 104.8°C (enthalpy of 204.71 J/g with an onset at 49.83°C) indicated an endothermic reaction, which could be due to the dehydration of HA. Moreover, a sharp characteristic peak was evident at 237.75°C (enthalpy 109.06 J/g with an onset at 228.37°C), indicating an exothermic reaction that corresponds to degradation, polymorphic conversion, crystallization, or crosslinking of HA (Figure 5). The melting point of HA was noted to be 108.39°C. Similarly, the DSC thermogram of the physical mixture of all ingredients showed a sharp peak at 97.65°C (enthalpy 5.0207 J/g with onset at 96.54 °C), indicating that the reaction was endothermic. Another sharp peak with an enthalpy of 8.5581 J/g and onset at 116.18°C was noted at 119.59°C. These peaks correspond to an exothermic reaction, which could be due to melting, polymorphic conversion, or denaturation of the individual components of the physical mixture. The melting point of physical mixture was 96.56°C. In the DSC thermogram of HA-PTX-TMX-CS-NPs, the distinct peaks associated with PTX, TMX, and TPP disappeared, suggesting a possible interaction or encapsulation of these components within polymeric matrix of CS, resulting in their distinct melting behavior (Figure 5). Moreover, a sharp exothermic peak at 246.08°C (enthalpy of 65.057 J/g with an onset at 240.21°C) corresponding to degradation, polymorphic conversion, crystallization, or crosslinking of HA was clearly visible in the DSC thermogram of HA-
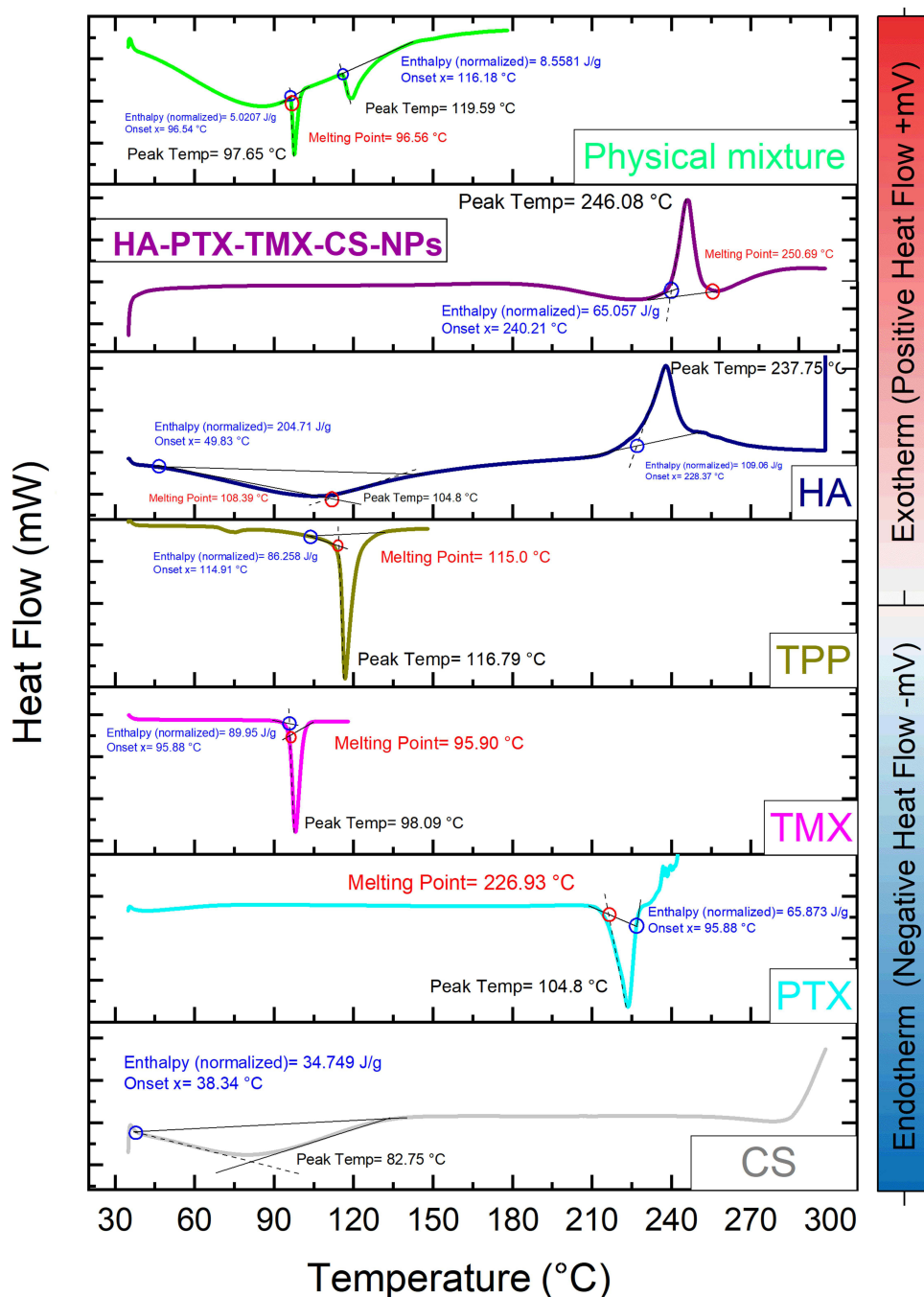
Figure 5 DSC analysis of HA-PTX-TMX-CS-NPs in comparison with the raw materials such as CS, PTX, TMX, TPP, and HA.

PTX-TMX-CS-NPs, confirming their successful surface decoration with HA. The melting point of HA-PTX-TMX-CS-NPs was 250.69°C, which was greater than that of all the individual components, indicating their greater thermal stability (Figure 5). These findings corroborated the successful encapsulation of PTX and TMX in the CS-NPs and their surface functionalization with HA.

Morphological Examination

Like other physicochemical properties (eg, PS, PDI, and ZP), the morphology or shape of NPs also play a crucial role in their colloidal stability, pharmacokinetics, cellular uptake, and biomedical efficacy. NPs exhibiting the relatively smaller
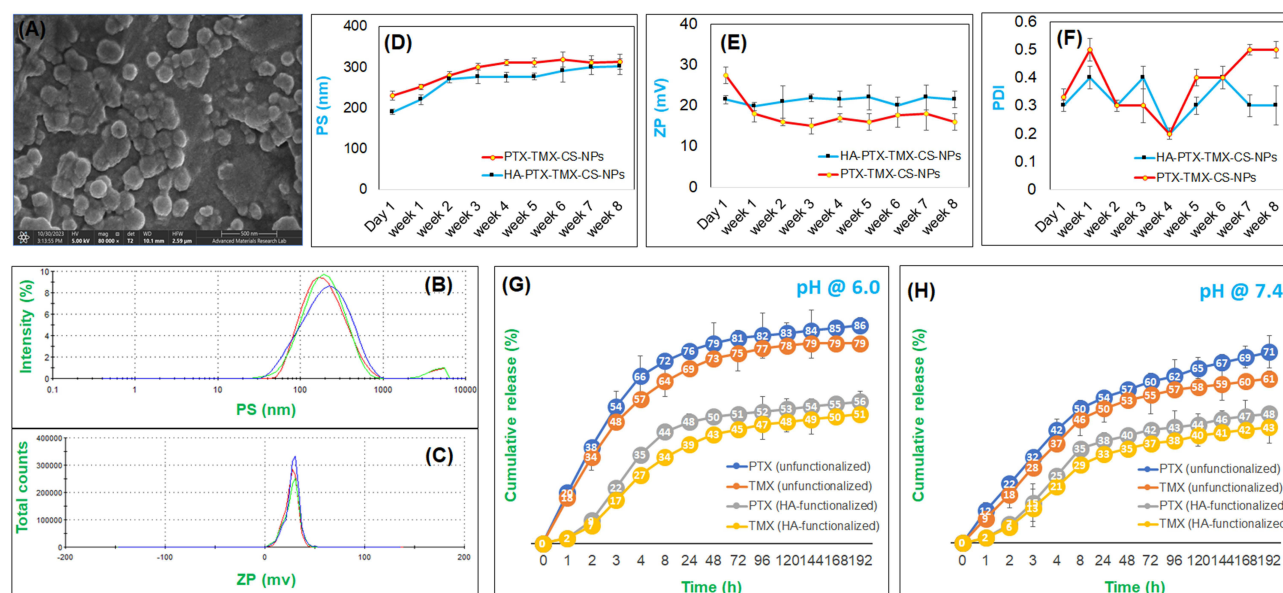
Figure 6 Morphology of HA-PTX-TMX-CS-NPs using the SEM (**A**), PS distribution (**B**) and ZP distribution (**C**) using the DLS analysis, colloidal stability of HA-PTX-TMX-CS-NPs in comparison with unfunctionalized PTX-TMX-CS-NPs in terms of mean PS (**D**), ZP (**E**), and PDI (**F**), and the percent cumulative release of PTX and TMX from HA-PTX-TMX-CS-NPs in comparison with unfunctionalized PTX-TMX-CS-NPs at pH 6.0 (**G**) and pH 7.4 (**H**).

size, spherical morphology, and smooth surface exhibit better colloidal stability, sustainable release, and greater absorption and distribution within the body because they can effectively pass-through various biological barriers.[42] In the context of targeted cancer therapy, smaller NPs with smooth morphology are more effectively taken up by the cancer cells and exhibit better anticancer efficacy.[43] Our SEM results indicated that the optimized HA-PTX-TMX-CS-NPs exhibited a spherical morphology with uniform size distribution ranging from approx. 170 to 200 nm (Figure 6A). The PS distribution depicted in the SEM image was relatively smaller than that measured by the DLS (Nano-ZS Zetasizer) (~230 nm) (Figure 6B). This was attributed to moderate shrinkage of the NPs because of the dehydration effect (evaporation of solvent) of freeze-drying process. Moreover, HA-PTX-TMX-CS-NPs showed a nominal aggregation, possibly due to surface coating with HA which might result in decrease in the surface charge of NPs (Figure 6C). Overall, our findings were in accordance with our research objectives of producing the NPs with smooth spherical morphology to achieve good cellular uptake into BC cells and TAMs.

Storage Stability

The colloidal stability of NPs during the storage is critically important for their intended applications. Therefore, it is pertinent to analyze possible interactions among the dispersed NPs as well as their interactions with the dispersed medium, as explained by the DLVO theory and the electrical double layer (EDL) phenomenon. The surface charge of NPs plays a key role in their interactions, leading to their potential reversible (flocculation) or irreversible (coagulation) agglomeration, which can significantly impact their storage stability, pharmacokinetics, therapeutic efficacy, and the safety.

Herein, we investigated the storage stability of our optimized HA-PTX-TMX-CS-NPs in comparison with unfunctionalized PTX-TMX-CS-NPs. In our previous studies, we established that storage of NPs in the refrigerator (2–8°C) preserves their physicochemical properties.[32,33] To confirm these findings, we evaluated the storage stability of both nanoformulations in the refrigerator (2–8°C) over a period of 8 weeks. The obtained results demonstrated a significant increase in the mean PS of unfunctionalized PTX-TMX-CS-NPs from ~190 nm to ~301 nm after 8 weeks of storage, suggesting a 58% increase in their mean PS (Figure 6D). Conversely, HA-PTX-TMX-CS-NPs showed lesser enlargement (36%) in their mean PS (~313 nm) after 8-week storage compared to freshly prepared NPs (~230 nm). The lower variation in the mean PS of HA-PTX-TMX-CS-NPs was attributed to lesser variation in their ZP from 21.5 mV to 19.8 mV compared to unfunctionalized PTX-TMX-CS-NPs in which the ZP was declined from 27.4 mV to 16 mV

(Figure 6E). Similarly, a lesser fluctuation was noted in the PDI of HA-PTX-TMX-CS-NPs compared to unfunctionalized NPs (Figure 6F). These findings highlighted the significance of HA-functionalization to preserve the physicochemical properties of developed NPs by preventing their undesired flocculation or coagulation.

In vitro Drug Release

The release of drugs from the polymeric matrix of NPs depends on the inherent properties of the matrix, polymer composition, and breakdown capability. There are three possible mechanisms through which drugs can be released from the polymeric matrix of NPs. The foremost mechanism is the diffusion, in which the encapsulated drugs diffuse out from the mesh of the polymeric network due to the concentration gradient. Depending upon the nature of the polymer, the encapsulated drug(s) may also be released from the polymeric matrix due to the erosion or degradation of the polymer in the biological environment. On the other hand, some polymers absorb fluid, swell, and ultimately release the encapsulated drug(s) in the release media. The swelling of the polymers can also be triggered by various factors such as change in the pH, temperature, light, and the ionic strength.[19,44]

Our results revealed that the optimized HA-PTX-TMX-CS-NPs exhibited a biphasic release pattern with an initial burst release within 8 h followed by the sustained release of the remaining drugs over a period of 8 days (Figure 6G and H). Interestingly, the release of both drugs was more pronounced at the acidic pH (pH 6.0) (Figure 6G) compared to physiological pH (pH 7.4) (Figure 6H) at 37°C. This was expected to be due to increase in the mesh size (swelling) of CS matrix at the acidic pH due to strong repulsion between amino groups ($-NH_3^+$) on the adjacent polymeric chains of CS. Notably, HA-PTX-TMX-CS-NPs displayed the slower release of the encapsulated drugs (~48% PTX and ~39% TMX) compared to unfunctionalized NPs (~76% PTX and ~69% TMX) within 24 h at the acidic pH, and a similar trend was noted at pH 7.4. This could be due to neutralization of the amino groups ($-NH_3^+$) on the contour of CS because of the adsorption of polyanionic HA, which possibly undermine the ionic repulsion between the similar charges and resulted in lesser swelling of CS network.[19] Another possible explanation could be the existence of an additional layer of HA coating on the surface of the NPs, which could have restricted the swelling of CS network and ultimately decreased the diffusion of the encapsulated drugs.[32,33] The total amount of drug released (PTX 56% and TMX 51%) from the HA-functionalized NPs after 192 h (8 days) was significantly lower than that released from the unfunctionalized PTX-TMX-CS-NPs (PTX 86% and TMX 79%) (Figure 6G and H). Moreover, we observed that the rate of TMX release from both NPs was relatively slower than PTX, which was attributed to hydrophilic nature of the TMX, resulting in good interactions with CS chains and ultimately restricting its release from the polymeric matrix.[19,44] The pH-responsive and sustained release behavior of HA-functionalized NPs signifies their potential for the targeted release of chemotherapeutic drugs in the TME (which is slightly acidic compared to healthy body tissues).[19]

Cytologic Evaluation

Cytotoxicity, IC$_{50}$, and Microscopy

Cytotoxicity assay is a fundamental biological method that is commonly used to evaluate the cytotoxicity and potency (IC$_{50}$) of bioactive compounds by analyzing the viability of treated cells. We conducted this assay to evaluate the anticancer efficacy of our optimized HA-PTX-TMX-CS-NPs using the MCF-7, SK-BR-3, and RAW 264.7 cells, and results were compared with unfunctionalized PTX-TMX-CS-NPs, HA-CS-NPs, blank CS-NPs, native drugs (PTX +TMX), and control (untreated) groups. The obtained results revealed that after 24 h of exposure the viability of MCF-7 cells treated with blank CS-NPs and HA-CS-NPs was greater than 90%, which indicated that CS-NPs were not toxic with or without HA-functionalization (Figure 7A). MCF-7 cells treated with free drugs (PTX-TMX) showed a noticeably higher cytotoxicity (~55% viability) than the control (100% viability), blank CS-NPs (>90%), and HA-CS-NPs (>90%). As anticipated, our optimized HA-PTX-TMX-CS-NPs exhibited superior cytotoxicity (~25%) against MCF-7 cells compared to unfunctionalized PTX-TMX-CS-NPs and other tested groups (Figure 7A). These results were also validated by estimating the IC$_{50}$ values, which indicated that HA-PTX-TMX-CS-NPs were more potent (IC$_{50}$ 5.0 µg) than unfunctionalized PTX-TMX-CS-NPs (IC$_{50}$ 6.2 µg) and free drugs (IC$_{50}$ 10.8 µg) (Figure 7D). Similarly, the viability of SK-BR-3 cells was greater than 90% after 24 h treatment with blank CS-NPs and HA-CS-NPs, indicating that these NPs were not cytotoxic (Figure 7B). Compared to control group (100% viability), SK-BR-3 cells treated with free drugs (PTX-TMX) showed 55% reduction in cell viability; however, cytotoxicity was pronounced when SK-BR-3 cells were treated with HA-PTX-TMX-CS-NPs. The viability of SK-BR-3 cells was decreased to ~35% and ~20% after
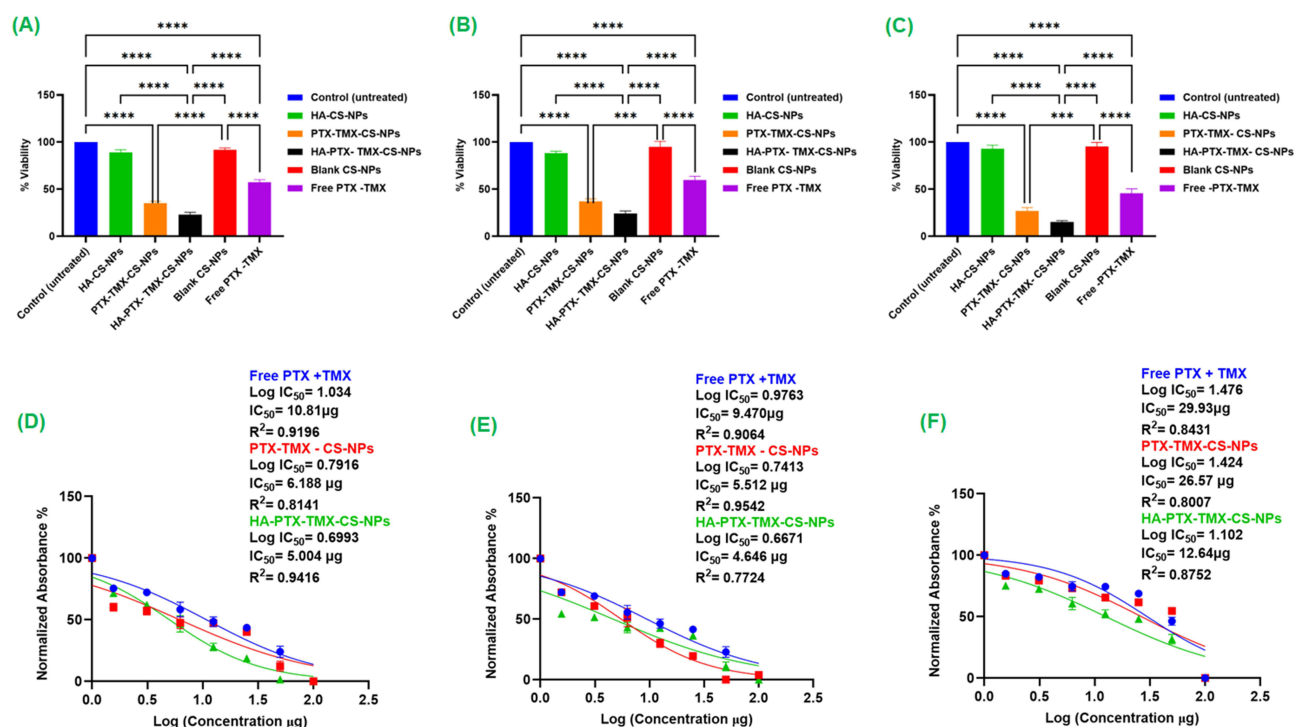
Figure 7 Cytotoxicity of HA-PTX-TMX-CS-NPs using the MCF-7 cells (**A**) cell viability and (**D**) IC$_{50}$, SK-BR-3 cells (**B**: cell viability and (**E**) IC$_{50}$), and RAW 264.7 cells (**C**) cell viability and (**F**) IC$_{50}$) in comparison with unfunctionalized PTX-TMX-CS-NPs, free drugs (PTX-TMX), blank CS-NPs, HA-CS-NPs, and control (untreated) groups. The statistical significance between tested groups is presented as ***$p < 0.0005$ and ****$p < 0.0001$.

treatment with PTX-TMX-CS-NPs and HA-PTX-TMX-CS-NPs, respectively (Figure 7B). The superior cytotoxic potential of the optimized HA-PTX-TMX-CS-NPs was also confirmed by calculating their IC$_{50}$ values, where HA-PTX-TMX-CS-NPs exhibited the lowest IC$_{50}$ value (4.6 µg) compared to PTX-TMX-CS-NPs (5.5 µg) and free drugs (9.5 µg) (Figure 7E). A similar pattern of cytotoxicity and IC$_{50}$ values was also evident in RAW 264.7 cells (Figure 7C and F). The superior cytotoxicity induced by NPs formulations, particularly HA-functionalized NPs, in BC cells and TAMs was anticipated to be due to their nanoscaled dimension, cationic charge, and spherical morphology, which enhanced their cellular uptake and induced cell apoptosis.[10,45]

Taken together, the cytotoxic potential of HA-PTX-TMX-CS-NPs was also analyzed using the light microscopy to detect any morphological changes (eg, shrinkage, cell membrane disruption, apoptotic bodies, etc.) and density of cell population of MCF-7, SK-BR-3 and RAW 264.7 cells (Figure 8A). The obtained microscopic images revealed no marked morphological aberrations in MCF-7 (Figure 8B), SK-BR-3 (Figure 8C), or RAW 264.7 cells (Figure 8D) after treatment with blank CS-NPs, HA-CS-NPs, and control (untreated) group. However, apparent cellular changes including cell shrinkage (which may be caused by leakage of cell content), swelling (which may be caused by osmosis), cell clustering, formation of apoptotic bodies, poor adherence, and decrease in cell density, were evident in MCF-7, SK-BR-3, and RAW 264.7 cells after treatment with free drugs (PTX-TMX). In consistence with cytotoxicity and IC$_{50}$ results, morphological aberrations were more pronounced when cells were treated with NPs, particularly the HA-PTX-TMX-CS-NPs, indicating their superior cytotoxic and apoptotic potential (Figure 8).

Cell Apoptosis

To further investigate the cytotoxic potential of our optimized HA-PTX-TMX-CS-NPs, we performed the cell apoptosis assay with MCF-7, SK-BR-3, and RAW 264.7 cells. In this double-staining assay, annexin V-FITC (which can bind to phosphatidylserine, PS) and 7-AAD (which intercalates into DNA fragments) were used to assess the translocation of the inner plasma membrane phospholipid PS to the outer layer of membrane in apoptotic cells. Our results indicated that compared with control (untreated) group, MCF-7 cells did not undergo considerable apoptosis (Q1-LR: early apoptosis; Q1-UR: early apoptosis) or necrosis (Q1-UL) after treatment with blank CS-NPs (81% viable Q1-LL cells) (Figure 9),
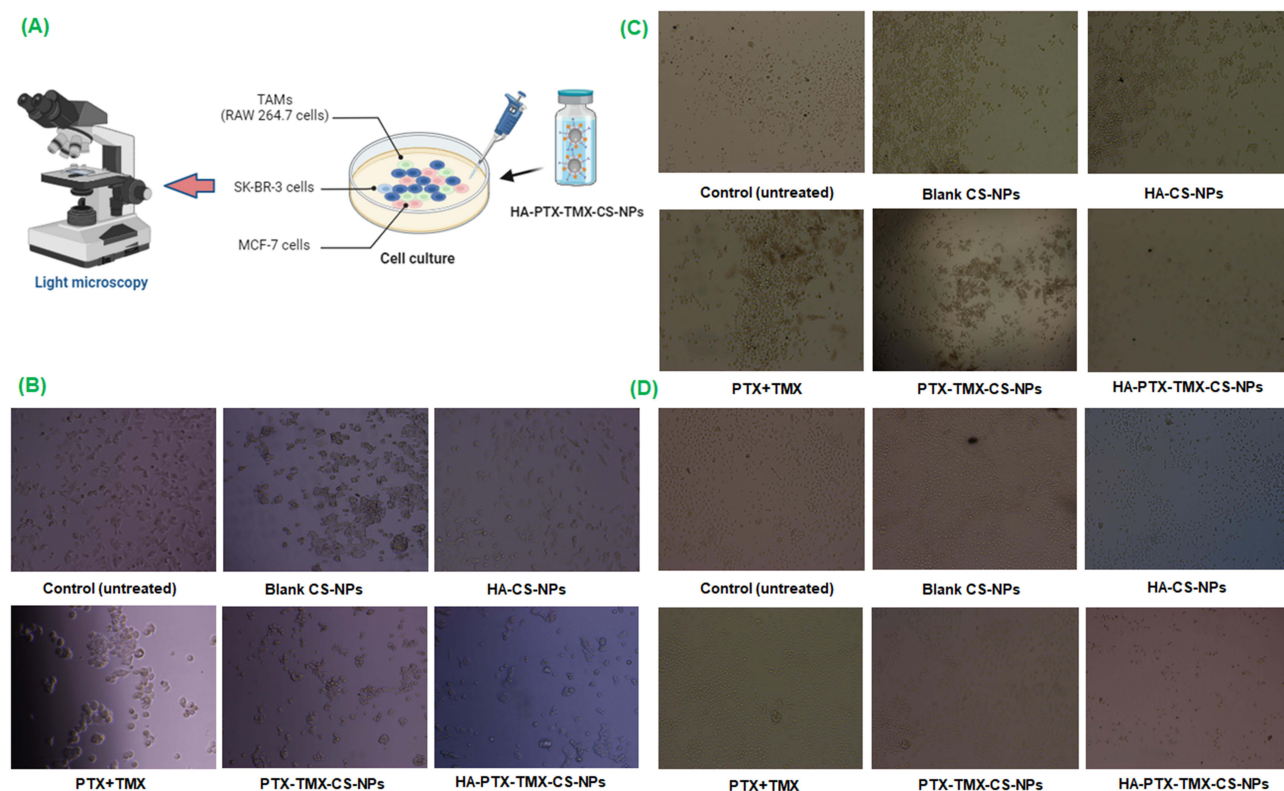
Figure 8 Cytotoxicity of HA-PTX-TMX-CS-NPs: flow diagram of cell morphology (**A**), cell morphology of MCF-7 cells (**B**), SK-BR-3 cells (**C**), and RAW 264.7 cells (**D**) using the light microscopy (magnification 10×, scale bar = 100 μm) in comparison with unfunctionalized PTX-TMX-CS-NPs, plain drugs (PTX+TMX), HA-CS-NPs, blank CS-NPs, and control (untreated) groups.
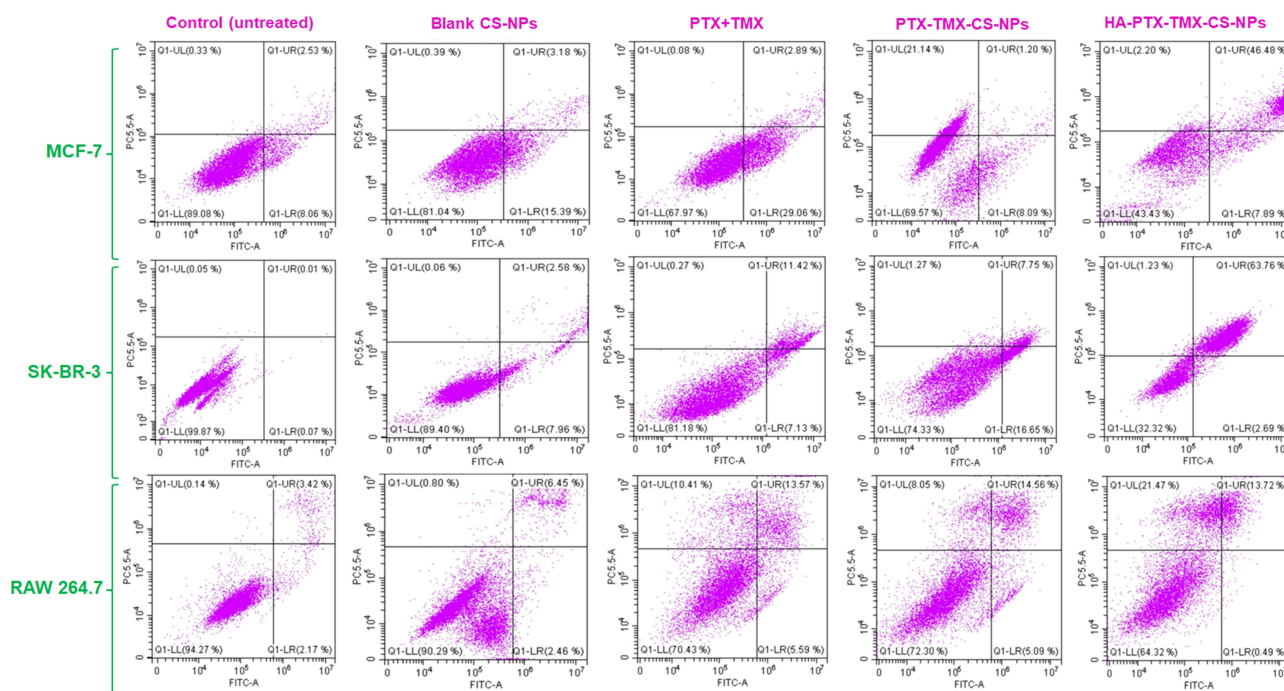

Figure 9 Apoptotic potential of HA-PTX-TMX-CS-NPs (10 μg/mL) against MCF-7, SK-BR-3, and RAW 264.7 cells according to annexin V-FITC/7-AAD dual-staining flow cytometry analysis compared to unfunctionalized PTX-TMX-CS-NPs, free PTX-TMX, blank CS-NPs, and control (untreated group) (Q1-LL: live cells, Q1-LR: early apoptosis, Q1-UR: late apoptosis, and Q1-UL: necrosis).

indicating their biocompatibility and non-toxicity against MCF-7 cells. In consistence with our results from the MTT assay, the percentage of live population of MCF-7 cells treated with blank CS-NPs was noticeably lower than the control group, which was likely due to CS which causes death of a small cell population. Notably, MCF-7 cells treated with HA-PTX-TMX-CS-NPs showed higher percentage of cells undergone late apoptosis (Q1-UR: 46.5%) compared to unfunctionalized PTX-TMX-CS-NPs (Q1-LR: 8%, Q1-UR: 1.2%, Q1-UL: 21%) and free drugs (Q1-LR: 29% and Q1-UR: 3%). The percentage of live cell population in HA-PTX-TMX-CS-NPs group was also lower (Q1-LL: ~43.4%) than unfunctionalized NPs (Q1-LL: ~70%) and free drug (Q1-LL: ~68%) groups (Figure 9).

The apoptotic potential of HA-PTX-TMX-CS-NPs was also validated in SK-BR-3 cells. SK-BR-3 cells treated with blank CS-NPs (Q1-LL: ~90, Q1-LR: 7%, Q1-UR: 2.5%, Q1-UL: 0%) showed no significant apoptosis or necrosis compared to control group (Q1-LL: ~99, Q1-LR: 0.07%, Q1-UR: 0.01%, Q1-UL: 0.05%) (Figure 9), indicating their biocompatibility and non-toxicity against SK-BR-3 cells. Like MCF-7 cells, SK-BR-3 cells treated with HA-PTX-TMX-CS-NPs also showed enhanced late apoptosis (Q1-UR: ~64%) compared to unfunctionalized NPs (Q1-UR: ~8%) and free drugs (Q1-UR: 11%). Moreover, the percentage of live cell population in HA-PTX-TMX-CS-NPs treated SK-BR-3 cells was lower (Q1-LL: ~32%) than the unfunctionalized NPs (Q1-LL: ~74%) and free drug (Q1-LL: ~81%) cultures (Figure 9).

Similarly, the apoptotic potential of optimized HA-PTX-TMX-CS-NPs was also verified in RAW 264.7 cells, and similar findings were observed. For example, like the control group (Q1-LL: ~94, Q1-LR: ~2%, Q1-UR: ~3%, Q1-UL: 0%), RAW 264.7 cells treated with blank CS-NPs showed no significant apoptosis (Q1-LL: ~90, Q1-LR: ~2.5%, Q1-UR: ~6.5%, Q1-UL: 0%). Though, the RAW 264.7 cells treated with HA-PTX-TMX-CS-NPs showed a comparable late apoptosis; however, their necrotic potential (Q1-UL: 21.5%) was superior to unfunctionalized NPs (Q1-UL: ~8%) and free drugs (Q1-UL: ~10.5%). Taken together, the percentage of live cell population in HA-PTX-TMX-CS-NPs treated RAW 264.7 cells was also noticeably lower (Q1-LL: ~64%) than the unfunctionalized NPs (Q1-LL: ~72%) and free drug (Q1-LL: ~70%) (Figure 9), which indicated their superior cytotoxic potential against the MCF-7, SK-BR-3, and RAW 264.7 cells. The superior apoptotic potential of HA-PTX-TMX-CS-NPs was attributed to their nanoscaled dimension, cationic charge, smooth spherical morphology, and enhanced cellular uptake through CD44-receptors-mediated endocytosis.[10,24,46]

Cell Cycle

Our findings from the previous experiments revealed that cytotoxic potential of HA-functionalized NPs is attributed to reduction in cell viability, morphological changes, and the induction of apoptosis in BC cells (MCF-7 and SK-BR-3) and TAMs (RAW 264.7); however, this experiment was conducted to evaluate the effect of HA-PTX-TMX-CS-NPs on different phases of the cell cycle. The results indicated that blank CS-NPs did not induce any change in the cell cycle of MCF-7 cells (G_0/G_1: ~62%, S: ~16%, G_2/M: ~21%) compared to the control (untreated) group (G_0/G_1: ~62%, S: ~16%, G_2/M: ~21%) (Figure 10). Following the treatment with free drugs (PTX-TMX), no significant changes were observed in the S (~18%) and G_2/M (~22.5%) phases of the cell cycle; however, a marked decrease in the percentage of MCF-7 subpopulation was evident in the G_0/G_1 phase (~54%) in comparison to the control group (G_0/G_1: ~62%), indicating that the free drugs predominantly induce cell cycle arrest at the G_1 phase. Moreover, an additional 5% of MCF-7 cells were arrested at the sub-G_1 phase, indicating the induction of apoptosis. On the other hand, MCF-7 cells treated with HA-PTX-TMX-CS-NPs exhibited mild changes in the cell cycle, including a nominal decrease in the percentage of cells in G_0/G_1 (~58%) and an increase in the percentage of cells in the S (~17%) and G_2/M (~23%) (G_0/G_1: ~62%, S: ~16%, G_2/M: ~21%) compared to the control group (Figure 10).

Similarly, the SK-BR-3 cells treated with HA-PTX-TMX-CS-NPs exhibited a noticeable decrease in the percentage of cell population in G_0/G_1 (~68%) and an increase in the percentage of cell population in the S (~16%) and G_2/M (~16%) phases compared to the control group (G_0/G_1: ~75%, S: ~14%, G_2/M: ~11%) (Figure 10). Moreover, we also evaluated the effect of HA-PTX-TMX-CS-NPs on the cell cycle of RAW 264.7 cells. The RAW 264.7 cells treated with HA-PTX-TMX-CS-NPs showed a slight increase in the percentage of cell population in the G_0/G_1 (~36%) and S (~25%) phases and a decrease in the cell population in the G_2/M (~36%) phase compared to the control group (G_0/G_1: ~32%, S: ~24%, G_2/M: ~40%) (Figure 10). These results indicate that the cytotoxic potential of HA-PTX-TMX-CS-NPs is mainly attributed to reduction in cell viability, morphological
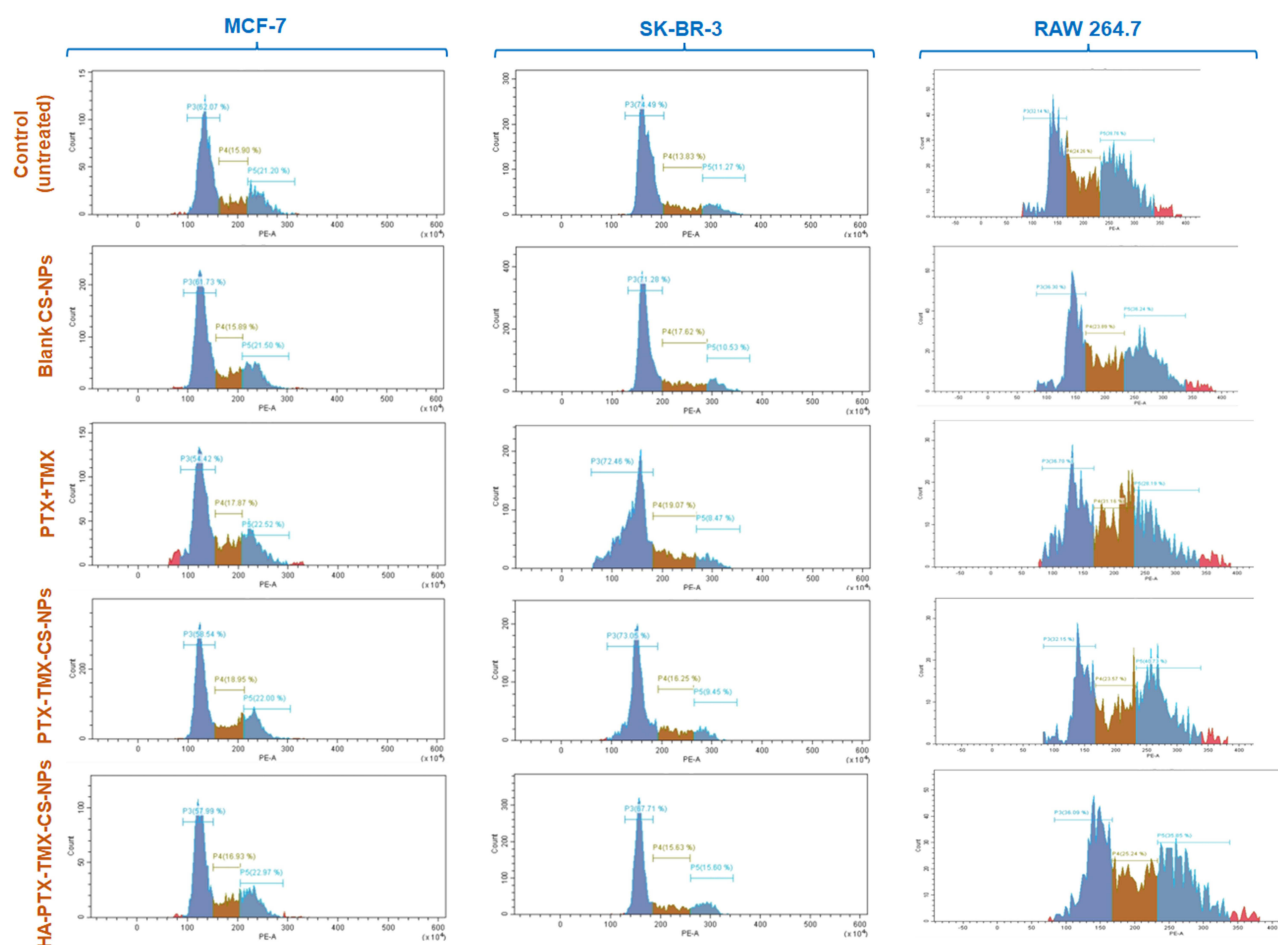
Figure 10 Cell cycle histograms of MCF-7, SK-BR-3, and RAW 264.7 cells treated with HA-PTX-TMX-CS-NPs, unfunctionalized PTX-TMX-CS-NPs, free drugs (PTX-TMX), blank CS-NPs, and control (untreated) using the flow cytometry.

aberrations, and induction of apoptosis, while inducing the modest changes in the cell cycle of MCF-7, SK-BR-3, and RAW 264.7 cells.

Cell Uptake

Cell uptake or internalization of chemotherapeutic agent(s) into cancer cells is a crucial step for inducing the apoptosis and enhancing the anticancer activity. To evaluate the cell internalization efficiency of HA-PTX-TMX-CS-NPs into MCF-7, SK-BR-3, and RAW 264.7 cells in comparison to the unfunctionalized NPs and free drugs, we used CLSM and flow cytometry. In this experiment, CMR, which is known for its bright green fluorescence, was chosen as a fluorophore due to its suitable emission spectrum. Similarly, DAPI (which appear as bright blue color) was used to stain the nuclei of cells, aiding in visualization of cell nuclei. The obtained CLSM images displayed a distinctive pattern of cellular uptake into MCF-7 cells after treatment with different test formulations. The absence of green fluorescence in the control group confirmed that MCF-7 cells were untreated. The low intensity of green fluorescence in MCF-7 cells treated with free CMR indicated poor internalization of CMR, which was expected to be due to its hydrophobicity and low penetrative ability (Figure 11A). On the other hand, MCF-7 cells treated with CMR-CS-NPs and HA-CMR-CS-NPs displayed bright green fluorescence, indicating that CMR was highly internalized when it was encapsulated into NPs. Notably, the fluorescence intensity was more pronounced in the MCF-7 cells treated with HA-CMR-CS-NPs (Figure 11A).

These findings were further confirmed using the flow cytometry (Figure 11B and C). Flow cytometry is a widely used technique in cell imaging and is commonly employed to investigate cellular uptake of fluorophores into various cells or tissues. Our resulting data showed that MCF-7 cells treated with the free CMR displayed only 6.85% uptake compared to
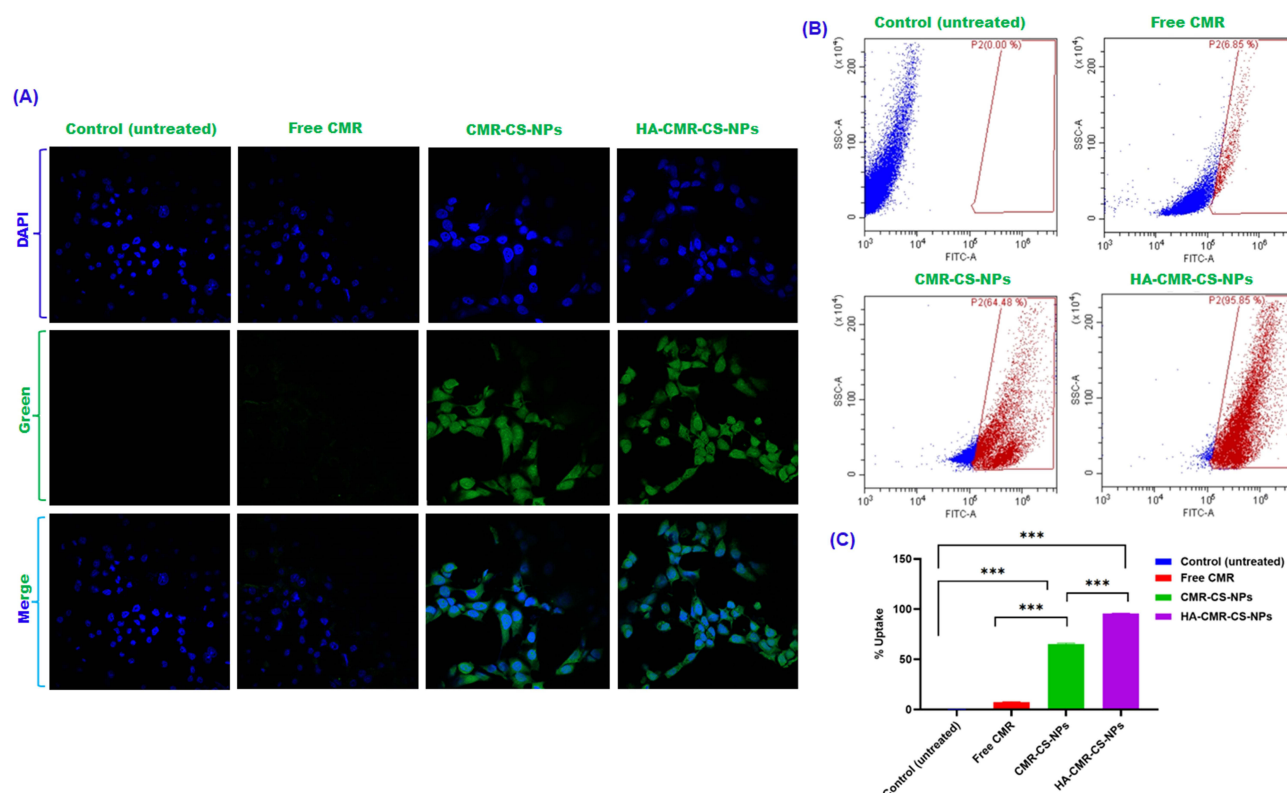
Figure 11 Cell uptake efficiency of HA-CMR-CS-NPs into MCF-7 cells using the CLSM (**A**) (magnification 60×, scale bar = 30 μm) and flow cytometry (**B** and **C**) in comparison with unfunctionalized CMR-CS-NPs, free CMR, and control (untreated) groups. The statistical significance between tested groups is presented as ***p < 0.0001.

virtually undetectable internalization in the control group (Figure 11B and C). The poor uptake of free CMR into MCF-7 cells is presumably due to its inherent hydrophobic nature and poor penetrability. On the other hand, a notable increase in the fluorescence intensity (~65%) was noted in the MCF-7 cells treated with CMR-CS-NPs, indicating the significance of NPs in enhancing the cellular uptake of encapsulated payload. In consistence with our results obtained from the CLSM, the efficiency of CMR uptake into MCF-7 cells was significantly higher (~96%) in HA-CMR-CS-NPs group (Figure 11B and C) compared to unfunctionalized NPs, free CMR, and control (untreated) groups. The superior intracellular uptake of HA-CMR-CS-NPs was attributed to HA-receptors-mediated endocytosis.[10,24,42]

The cell uptake efficiency of HA-CMR-CS-NPs was also validated in SK-BR-3 cells compared to unfunctionalized CMR-CS-NPs, free CMR, and control groups. The obtained CLSM images indicated that SK-BR-3 cells treated with free CMR displayed lower fluorescence intensity (faint green color), indicating its poor cellular uptake due to its hydrophobic nature and low permeability (Figure 12A). On the other hand, the CLSM images of SK-BR-3 cells treated with HA-CMR -CS-NPs and CMR-CS-NPs depicted a notably higher fluorescence intensity, indicating NPs potential to enhance the intracellular trafficking of CMR due to their nanoscaled dimension, surface chemistry, and smooth spherical morphology. Like MCF-7 cells, the SK-BR-3 cells treated with HA-CMR-CS-NPs depicted noticeably higher uptake compared to unfunctionalized CMR-CS-NPs, free CMR, and control (untreated) groups. The striking uptake of CMR into SK-BR-3 cells obtained with HA-functionalized NPs was attributed to CD44-receptors-mediated endocytosis, along with their nanoscaled dimension, cationic charge, and smooth spherical morphology (Figure 12A).[47,48] These results were also verified using the flow cytometry (Figure 12B and C). The SK-BR-3 cells treated with free CMR exhibited approximately 10% uptake compared to almost 0% uptake in the control group (Figure 12B and 12C). On the other hand, SK-BR -3 cells treated with CMR-CS-NPs exhibited notably higher cellular uptake (~67%) compared to free CMR and control groups, indicating the ability of CS-NPs to promote the cell internalization of encapsulated payload. The cell uptake of CMR into SK-BR-3 cells was highest (~96%) when treated with HA-CMR-CS-NPs (Figure 12B and C) compared to unfunctionalized NPs, free CMR, and control groups. The superior cellular uptake of HA-CMR-CS-NPs was attributed to
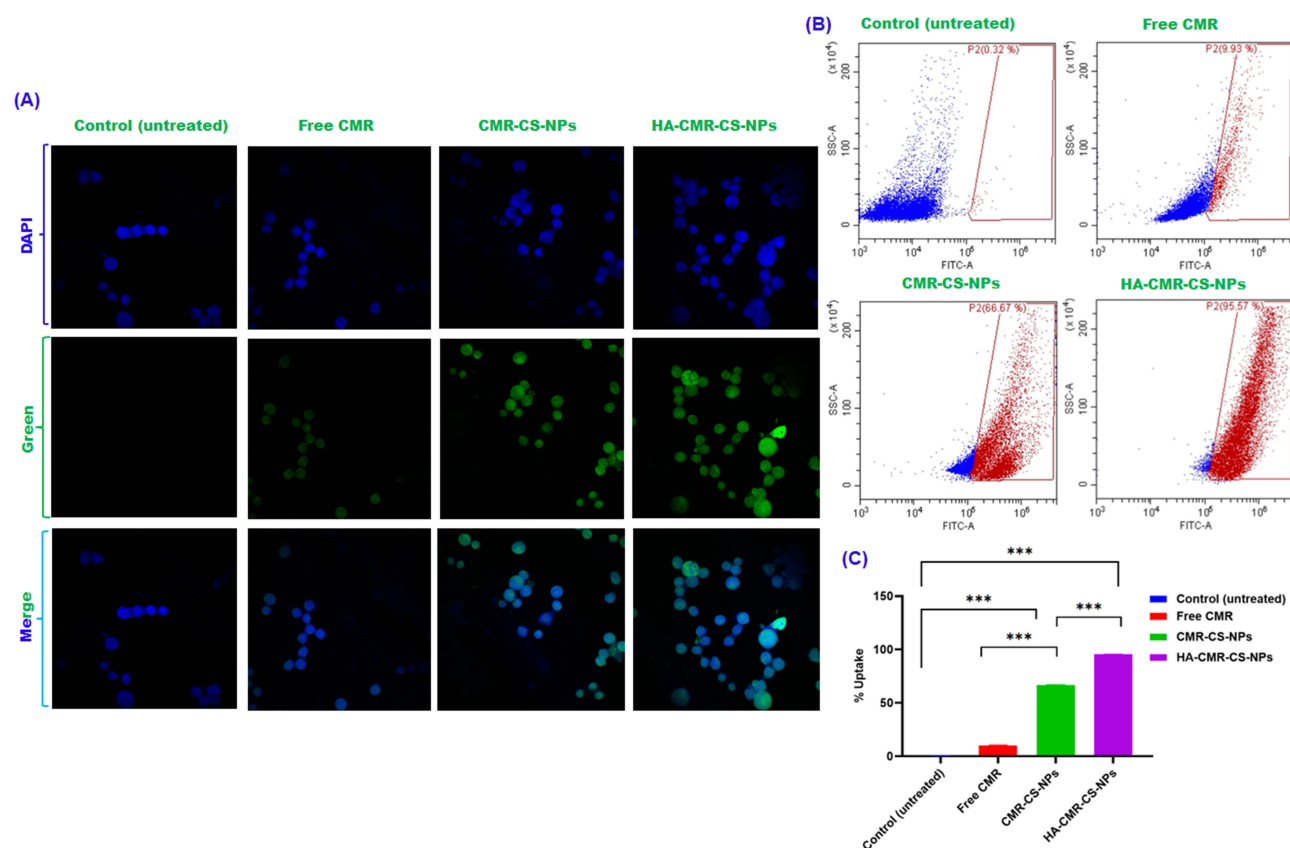
Figure 12 Cell uptake efficiency of HA-CMR-CS-NPs into SK-BR-3 cells using the CLSM (**A**) (magnification 60×, scale bar = 30 μm) and flow cytometry (**B** and **C**) in comparison with unfunctionalized CMR-CS-NPs, free CMR, and control (untreated) groups. The statistical significance between tested groups is presented as ***p < 0.0001.

CD44-receptors-mediated endocytosis into SK-BR-3 cells, highlighting the significance of HA-functionalization for targeted delivery of therapeutic payload to BC cells.[24,46]

Additionally, we validated the cell uptake efficiency of HA-CMR-CS-NPs into RAW 264.7 cells in comparison with unfunctionalized CMR-CS-NPs, free CMR, and control groups. While control group depicted no fluorescence, the RAW 264.7 cells treated with free CMR exhibited lower fluorescence intensity (dizzy green color), indicating the poor cellular uptake efficiency of free CMR due to its inherent hydrophobic nature and low permeability (Figure 13A). In comparison with free CMR, the RAW 264.7 cells treated with CMR-CS-NPs depicted higher fluorescent intensity, demonstrating the potential of NPs for enhancing the cellular uptake of hydrophobic compounds. Like MCF-7 and SK-BR-3 cells, the RAW 264.7 cells also displayed highest fluorescence intensity (bright green color) when treated with HA-CMR-CS-NPs compared to unfunctionalized CMR-CS -NPs, free CMR, and control (untreated) group (Figure 13A). These results were also confirmed using the flow cytometry (Figure 13B and C). The obtained results illustrated that RAW 264.7 cells treated with free CMR exhibited only 7% uptake compared to control group, which showed no uptake (Figure 13B and C). The uptake efficiency was significantly (p < 0.0001) enhanced (~66%) when RAW 264.7 cells were treated with CMR-CS-NPs compared to free CMR and control groups. These findings agreed with CLSM results, indicating that NPs boost the intracellular delivery of encapsulated payload. The cellular uptake of CMR into RAW 264.7 cells was strikingly high (~96%) after treatment with HA-CMR-CS-NPs (Figure 13B and C). The superior cellular uptake of HA-CMR-CS-NPs was attributed to CD44-receptors-mediated endocytosis, highlighting the significance of HA-functionalization for targeted delivery of therapeutic payload to TAMs.[24,46]

Scratch Assay

Metastasis is one of the critical attributes of the advanced stage BC, which is associated with low survival rate and high recurrence potential.[6] The migration of cancer cells from the primary tumor sites to the distant parts of the body is a key
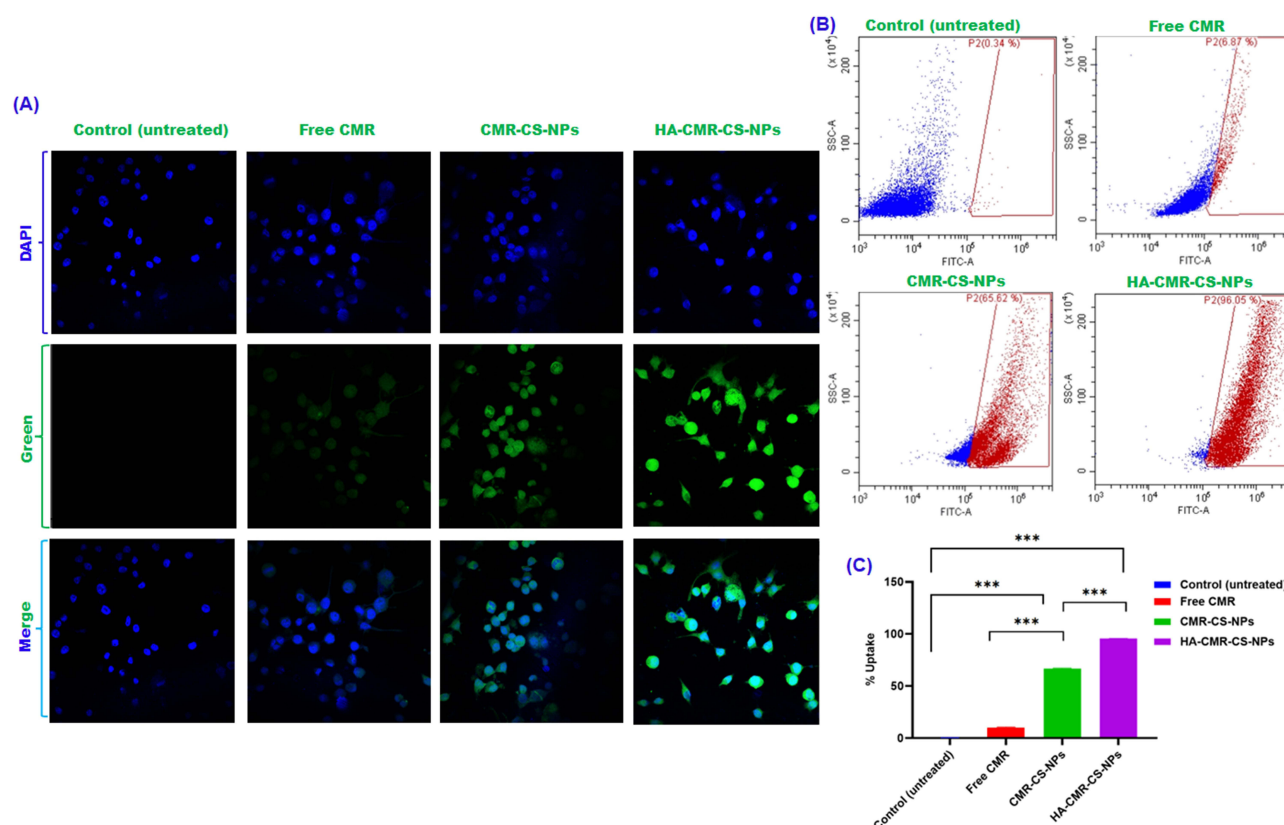
Figure 13 Cell uptake efficiency of HA-CMR-CS-NPs into RAW 264.7 cells using the CLSM (**A**) (magnification 60×, scale bar = 30 μm) and flow cytometry (**B** and **C**) in comparison with unfunctionalized CMR-CS-NPs, free CMR, and control (untreated) groups. The statistical significance between tested groups is presented as ***p < 0.0001.

factor in the development and progression of BC. Herein, we performed a scratch assay to evaluate the antimetastatic efficacy of our optimized HA-PTX-TMX-CS-NPs by analyzing the migration of MCF-7 and SKBR-3 cells to scratch-induced gaps in their cell monolayers. For comparison, the microscopy images of scratch-induced gaps were captured at three different time intervals (0 h, 24 h, and 48 h). Our results revealed that MCF-7 cells with no treatment (control) showed good migration with consistent increase in the closure of scratch-induced gap after 24 h and 48 h (Figure 14A). The MCF-7 cells treated with free drugs (PTX-TMX) also showed obvious migration to scratch-induced gap, indicating their low antimetastatic efficacy. On the other hand, a clearly visible scratch-induced gap was evident in the MCF-7 cells treated with NPs, particularly the HA-PTX-TMX-CS-NPs (Figure 14A). MCF-7 cells treated with unfunctionalized PTX-TMX-CS-NPs displayed a few cell colonies in the scratch-induced gap after 48 h, which indicated that PTX-TMX-CS-NPs exhibited higher antimetastatic efficacy compared to the free drugs and the control groups. Notably, no apparent cell colonies along with poor migration were evidenced in the MCF-7 cells treated with HA-PTX-TMX-CS-NPs after 24 h and 48 h, demonstrating their exceptional antimetastatic efficacy.[49,50] For quantification, the obtained results were also analyzed in terms of gap closure rate (%), and it was evident that MCF-7 cells treated with HA-PTX-TMX-CS-NPs displayed lowest gap closure rates at 24 h (<5%) and 48 h (<3%) compared to the unfunctionalized NPs (~10% at 24 h and ~7% at 48 h), free drugs (~20% at 24 h and ~35% at 48 h), and the control groups (~35% at 24 h and 55% at 48 h). These results confirmed the superior antimetastatic potential of HA-PTX-TMX-CS-NPs compared to unfunctionalized NPs, free drugs, and control groups (Figure 14B). The patronizing antimetastatic efficacy of HA-PTX-TMX-CS-NPs was attributed to their superior cytotoxicity, induction of apoptosis, dysregulation of cell cycle, and pronounced cell internalization efficiency through CD44-receptors-mediated endocytosis.

Like MCF-7 cells, the SKBR-3 cells treated with HA-PTX-TMX-CS-NPs also showed the superior antimetastatic efficacy compared to other treatment groups. The SK-BR-3 cells that received no treatment (control) displayed immense migratory potential with a consistent increase in the extent of scratch-induced gap after 24 h and 48 h (Figure 15A). The
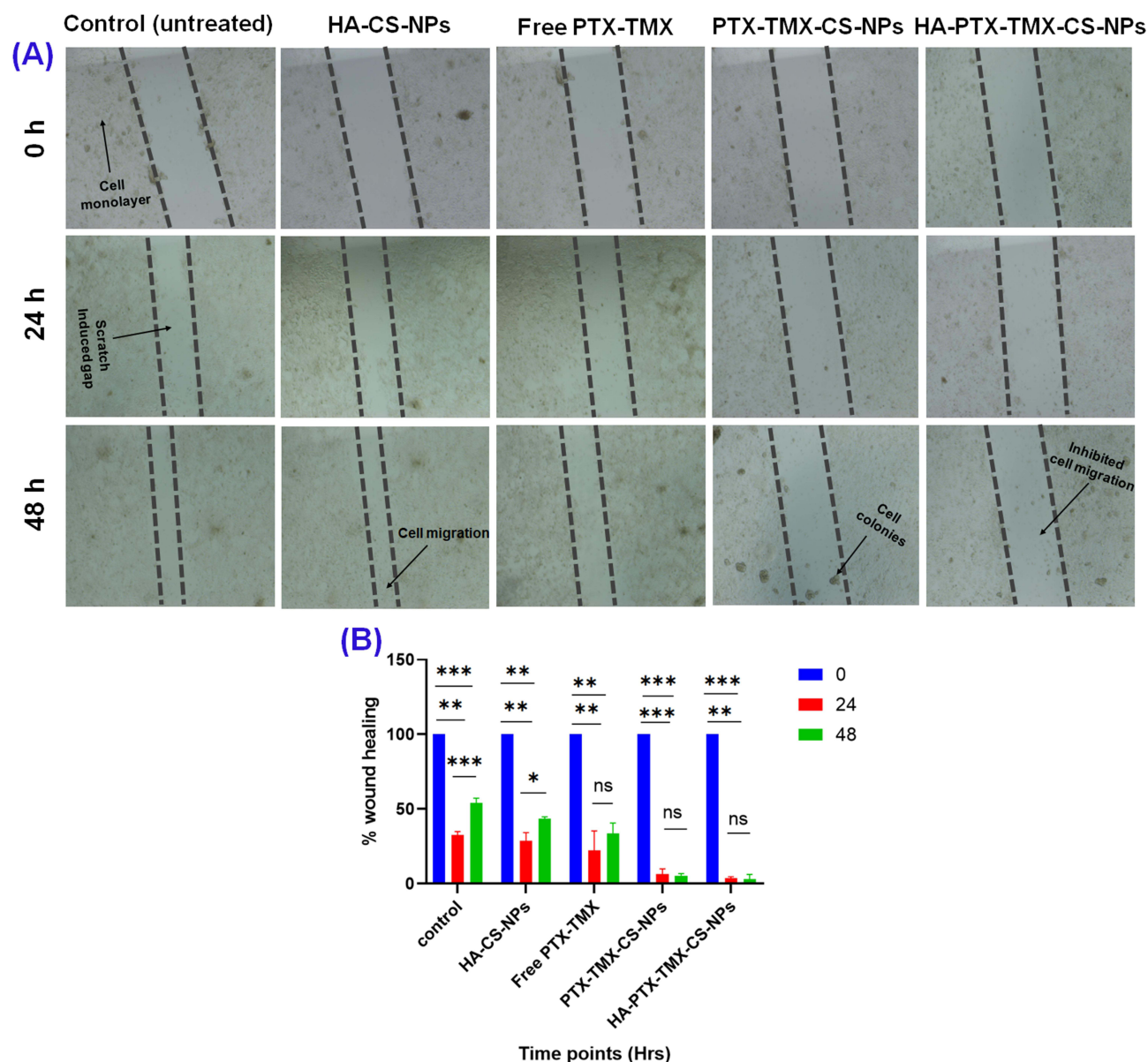
Figure 14 Antimetastatic efficacy of HA-PTX-TMX-CS-NPs against MCF-7 cells using the light microscopy (magnification 4×, scale bar = 150 μm) (**A**) and scratch-induced gap closure rate (%) (**B**) in comparison with unfunctionalized PTX-TMX-CS-NPs, free drugs (PTX-TMX), and control (untreated) groups. The statistical significance between tested groups is presented as ns (not significant), * p < 0.05, ** p < 0.005, and *** p < 0.001.

migratory potential of SK-BR-3 cells decreased after treatment with free drugs (PTX-TMX) and HA-CS-NPs, demonstrating their good antimetastatic efficacies. Notably, in comparison with free drug, HA-CS-NPs, and control groups, the SK-BR-3 cells treated with NPs exhibited poor migration, demonstrating their promising antimetastatic potential.[49,50] The resulting data was also statistically analyzed in terms of gap closure rate (%), and it was evident that the SK-BR-3 cells with no treatment (control) exhibited the highest gap closure rate (~50% at 24 h and ~60% at 48 h). On the other hand, the SK-BR-3 cells treated with free drugs (~15% at 24 h and ~25% at 48 h) and HA-CS-NPs (~15% at 24 h and ~25% at 48 h) showed lower gap closure rates compared to control group, indicating the modest antimetastatic potential of these treatments. Notably, the lowest and comparable gap closure rates were detected in SK-BR-3 cells treated with HA-PTX-TMX-CS-NPs (~5% at 24 h and ~7% at 48 h) and PTX-TMX-CS-NPs (~7% at 24 h and ~10% at 48 h). These results validated the superior antimetastatic potential of NPs, particularly the HA-PTX-TMX-CS-NPs, in comparison with free drugs, HA-CS-NPs, and control groups (Figure 15B). The exceptional antimetastatic efficacy of HA-PTX-TMX
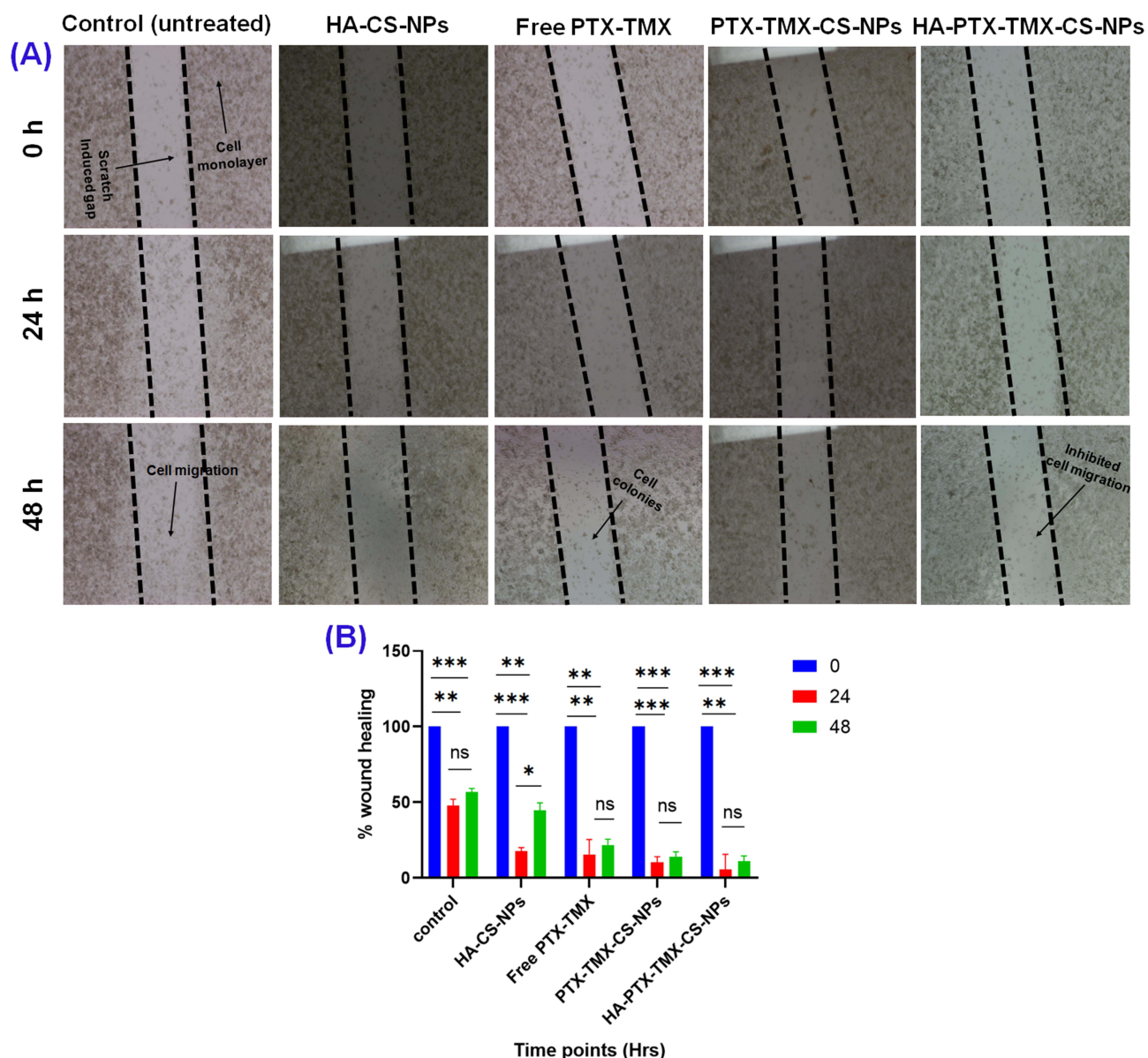
Figure 15 Antimetastatic efficacy of HA-PTX-TMX-CS-NPs against SK-BR-3 cells using the light microscopy (magnification 4×, scale bar = 150 μm) (**A**) and scratch-induced gap closure rate (%) (**B**) in comparison with unfunctionalized PTX-TMX-CS-NPs, free drugs (PTX-TMX), and control (untreated) groups. The statistical significance between tested groups is presented as ns (not significant), * $p < 0.05$, ** $p < 0.005$, and *** $p < 0.001$.

-CS-NPs was attributed to their superior cytotoxicity, induction of apoptosis, effect on cell cycle, and pronounced cell internalization efficiency through CD44-receptors-mediated endocytosis compared to unfunctionalized NPs, free drugs, and control (untreated) groups.

Conclusion

In this research, we hypothesized that the surface functionalization of CS-NPs with HA could be a promising strategy for targeted delivery of chemotherapeutics to BC cells and TAMs through CD44-receptors-mediated endocytosis. Hence, we fabricated PTX/TMX co-loaded CS-NPs using the ionic gelation method and functionalized their surfaces with HA for their targeted delivery through the CD44-receptors, which are abundantly expressed on BC (MCF-7 and SK-BR-3) and RAW 264.7 cells. The physicochemical properties (ie, particle size, zeta potential, morphology, surface chemistry, etc.) of NPs play a crucial role in their intracellular delivery; therefore, we employed a quality-by-design approach using the

Design Expert® software for the optimization of fabricated NPs. A robust relationship between studied factors (CMAs and CPPs) and physicochemical properties of NPs suggested that drug concentration, incubation time, and homogenization are essential factors that should be considered when designing the NPs formulations. Based on our optimization results, the PTX-TMX-CS-NPs produced with 0.5 mg/mL drug concentration and incubated for 60 min without homogenization exhibited the most desirable physicochemical features. The optimized HA-PTX-TMX-CS-NPs exhibited the mean PS of 230 ± 21 nm, PDI of 0.30 ± 0.04, ZP of 21.5 ± 3.4 mV, and high %EE of PTX 71.9 ± 5.2% and TMX 96.6 ± 8.8. The successful loading of PTX and TMX into the polymeric matrix of CS-NPs and their functionalization with HA were verified through the FTIR and DSC analyses. The SEM analysis of the optimized HA-PTX-TMX-CS-NPs depicted a smooth spherical morphology and nanoscaled dimension (170 to 200 nm) with nominal tendency for aggregation, which was likely due to the dehydration effect of lyophilization and the surface coating with HA. The insignificant variations in the mean PS, PDI, and ZP of HA-PTX-TMX-CS-NPs compared to unfunctionalized PTX-TMX-CS-NPs during their storage (PBS, pH 7.4) for 8-week at 2–8°C demonstrated that HA-functionalization improves the good colloidal stability of NPs. The in vitro release study revealed that HA-PTX-TMX-CS-NPs exhibited pH-responsive sustained release behavior, which signifies their ability to selectively deliver the encapsulated drugs into the TME (which is slightly acidic compared to healthy body tissues). The lowest cell viability witnessed in MCF-7 (~25%), SK-BR-3 (~20%), and RAW 264.7 cells (~20%) along with lowest IC_{50} values for MCF-7 (~5.0 μg), SK-BR-3 (4.6 μg), and RAW 264.7 cells (12.6 μg) certified that our optimized HA-PTX-TMX-CS-NPs exhibited powerful cytotoxic potential against the BC and TAMs. To elucidate the mechanism of cytotoxicity induced by HA-functionalized NPs, a series of experiments including cell apoptosis, cell cycle, and cellular uptake, were conducted. The confocal laser scanning microscopy and flow cytometry results demonstrated that the HA-PTX-TMX-CS-NPs possess exceptional ability to induce apoptosis, dysregulate cell cycle, and enhance cell internalization compared to unfunctionalized NPs, free drug, and control (untreated) groups. Taken together, HA-PTX-TMX-CS-NPs displayed a promising antimetastatic efficacy by downregulating the proliferation and migration of MCF-7 and SK-BR-3 cells within scratch-induced gaps. These findings confirm that HA-functionalization of CS-NPs is a promising targeting strategy to eliminate BC cells and TAMs with an ultimate abolishment of disease progression and metastasis. Based on our findings, we anticipate that HA-PTX-TMX-CS-NPs could be a promising anticancer nanomedicine for the treatment of BC and other types of cancer; however, substantial in vivo studies using the tumor-bearing animal models, pharmacokinetics, and safety evaluations are highly warranted prior to further development of this nanomedicine for the clinical translation.

Ethics Approval and Consent to Participate
This research was exempted from the ethical approval because this project does not involve primary cell lines (cultivation of cells from tissue), tissues, animals, or human.

Acknowledgment

Author Contributions
All authors made a significant contribution to the work reported, whether that is in the conception, study design, execution, acquisition of data, analysis and interpretation, or in all these areas; took part in drafting, revising or critically reviewing the article; gave final approval of the version to be published; have agreed on the journal to which the article has been submitted; and agree to be accountable for all aspects of the work.

Funding

Disclosure

The authors report no conflicts of interest in the present work.

References

1. Obeagu EI, Obeagu GU. Breast cancer: a review of risk factors and diagnosis. *Medicine*. 2024;103(3):e36905. doi:10.1097/MD.0000000000036905
2. Cömert D, van Gils CH, Veldhuis WB, Mann RM. Challenges and changes of the breast cancer screening paradigm. *J Magn Reson Imaging*. 2023;57(3):706–726. doi:10.1002/jmri.28495
3. Bhushan A, Gonsalves A, Menon JU. Current state of breast cancer diagnosis, treatment, and theranostics. *Pharmaceutics*. 2021;13(5):723. doi:10.3390/pharmaceutics13050723
4. Nounou MI, ElAmrawy F, Ahmed N, Abdelraouf K, Goda S, Syed-Sha-Qhattal H. Breast cancer: conventional diagnosis and treatment modalities and recent patents and technologies. *Breast Cancer*. 2015;9(Suppl 2):17–34. doi:10.4137/BCBCR.S29420
5. Koh J, Kim M. Introduction of a new staging system of breast cancer for radiologists: an emphasis on the prognostic stage. *Korean J Radiol*. 2019;20(1):69–82. doi:10.3348/kjr.2018.0231
6. Yang Z, Shi F, Yongchao L, et al. Exosome as non-invasive prognostic and diagnostic biomarker and nanovesicle for targeted therapy of non-small cell lung carcinoma. *Chem Eng J*. 2024;480:148160. doi:10.1016/j.cej.2023.148160
7. Gao J, Liang Y, Wang L. Shaping polarization of tumor-associated macrophages in cancer immunotherapy. *Front Immunol*. 2022;13:888713. doi:10.3389/fimmu.2022.888713
8. Rios de la Rosa JM, Tirella A, Tirelli N. Receptor-targeted drug delivery and the (many) problems we know of: the case of CD44 and hyaluronic acid. *Adv Biosyst*. 2018;2(6):1800049. doi:10.1002/adbi.201800049
9. de la Rosa JM R, Tirella A, Gennari A, Stratford IJ, Tirelli N. The CD44-mediated uptake of hyaluronic acid-based carriers in macrophages. *Adv Healthc Mater*. 2017;6(4). doi:10.1002/adhm.201601012
10. de la Rosa JM R, Pingrajai P, Pelliccia M, et al. Binding and internalization in receptor-targeted carriers: the complex role of CD44 in the uptake of hyaluronic acid-based nanoparticles (siRNA delivery). *Adv Healthc Mater*. 2019;8(24):e1901182. doi:10.1002/adhm.201901182
11. Baskar R, Lee K, Yeo R, Yeoh K. Cancer and radiation therapy: current advances and 1100 future directions. *Int J Med Sci*. 2012;9(3):193–199.1101. doi:10.7150/ijms.3635
12. Cai F, Luis M, Lin X, et al. Anthracycline-induced cardiotoxicity in the chemotherapy treatment of breast cancer: preventive strategies and treatment (Review). *Mol Clin Oncol*. 2019;11(1):15–23. doi:10.3892/mco.2019.1854
13. Suhail M, Saulat F, Khurram H, et al. Attitude and practice related to chemotherapy among cancer patients. *Inquiry*. 2024;61:469580241246460. doi:10.1177/00469580241246460
14. Hussain Z, Khan S, Imran M, Sohail M, Shah SWA, de Matas M. PEGylation: a promising strategy to overcome challenges to cancer-targeted nanomedicines: a review of challenges to clinical transition and promising resolution. *Drug Deliv Transl Res*. 2019;9(3):721–734. doi:10.1007/s13346-019-00631-4
15. Hussain Z, Rahim MA, Jan N, et al. Cell membrane cloaked nanomedicines for bio-imaging and immunotherapy of cancer: improved pharmacokinetics, cell internalization and anticancer efficacy. *J Control Release*. 2021;335:130–157. doi:10.1016/j.jconrel.2021.05.018
16. Al-Shadidi JRMH, Hussain Z, Ahmed IS, Rawas-Qalaji M, Thu HE, Khan S. Polyethylene glycol-mediated functionalization of nanodelivery systems for improving their pharmacokinetic profile and anticancer efficacy. *Int J Polym Mater Polym Biomater*. 2024;1–19. doi:10.1080/00914037.2024.2383413
17. Zhang J, Sun J, Li C, Qiao H, Hussain Z. Functionalization of curcumin nanomedicines: a recent promising adaptation to maximize pharmacokinetic profile, specific cell internalization and anticancer efficacy against breast cancer. *J Nanobiotechnology*. 2023;21(1):106. doi:10.1186/s12951-023-01854-x
18. Moti LAA, Hussain Z, Thu HE, Khan S, Sohail M, Sarfraz RM. Multi-functionalization, a promising adaptation to overcome challenges to clinical translation of nanomedicines as nano-diagnostics and nano-therapeutics for breast cancer. *Curr Pharm Des*. 2021;27(43):4356–4375. doi:10.2174/1381612827666210830092539
19. Al-Shadidi JRMH, Al-Shammari S, Al-Mutairi D, Alkhudhair D, Thu HE, Hussain Z. Chitosan nanoparticles for targeted cancer therapy: a review of stimuli-responsive, passive, and active targeting strategies. *Int J Nanomed*. 2024;19:8373–8400. doi:10.2147/IJN.S472433
20. Haider M, Zaki KZ, El Hamshary MR, Hussain Z, Orive G, Ibrahim HO. Polymeric nanocarriers: a promising tool for early diagnosis and efficient treatment of colorectal cancer. *J Adv Res*. 2022;39:237–255. doi:10.1016/j.jare.2021.11.008
21. Safdar MH, Hussain Z, Abourehab MAS, Hasan H, Afzal S, Thu HE. New developments and clinical transition of hyaluronic acid-based nanotherapeutics for treatment of cancer: reversing multidrug resistance, tumor-specific targetability and improved anticancer efficacy. *Artif Cells Nanomed Biotechnol*. 2018;46(8):1967–1980. doi:10.1080/21691401.2017.1397001
22. Haider M, Elsherbeny A, Pittalà V, et al. Nanomedicine strategies for management of drug resistance in lung cancer. *Int J mol Sci*. 2022;23(3):1853. doi:10.3390/ijms23031853
23. Rahim MA, Jan N, Khan S, et al. Recent advancements in stimuli responsive drug delivery platforms for active and passive cancer targeting. *Cancers*. 2021;13(4):670. doi:10.3390/cancers13040670
24. Hussain Z, Hamzeh Akbari A, Husam Barbuor S, Salman Dawood Alshetiwi D, Saad Ahmed I, Rawas-Qalaji M. Hyaluronic acid based functionalization of nanodelivery systems: a promising strategy for CD44-receptors-mediated targeted therapy of lung cancer. *J Drug Delivery Sci Technol*. 2024;101(Part A):106183. doi:10.1016/j.jddst.2024.106183
25. Khan S, Imran M, Tahir Butt T, et al. Curcumin based nanomedicines as efficient nanoplatform for treatment of cancer: new developments in reversing cancer drug resistance, rapid internalization, and improved anticancer efficacy. *Trends Food Sci Technol*. 2018;80:8–22. doi:10.1016/j.tifs.2018.07.026
26. Chen H, Luo X, Huang Q, et al. Platelet membrane fusion liposome loaded with type I AIE photosensitizer to induce chemoresistance cancer pyroptosis and immunogenic cell death for enhancing cancer immunotherapy. *Chem Eng J*. 2023;476:146276. doi:10.1016/j.cej.2023.146276
27. Zhang T, Pan Y, Suo M, et al. Photothermal-triggered sulfur oxide gas therapy augments type i photodynamic therapy for potentiating cancer stem cell ablation and inhibiting radioresistant tumor recurrence. *Adv Sci*. 2023;10(29):e2304042. doi:10.1002/advs.202304042

28. Ning S, Lyu M, Zhu D, et al. Type-I AIE photosensitizer loaded biomimetic system boosting cuproptosis to inhibit breast cancer metastasis and rechallenge. *ACS Nano*. 2023;17(11):10206–10217. doi:10.1021/acsnano.3c00326

29. Ning S, Zhang T, Lyu M, et al. A type I AIE photosensitiser-loaded biomimetic nanosystem allowing precise depletion of cancer stem cells and prevention of cancer recurrence after radiotherapy. *Biomaterials*. 2023;295:122034. doi:10.1016/j.biomaterials.2023.122034

30. Oscar E-R, Paulina F-V, Samantha J-X, Carlos GG-T, Susana M-E, David Q-G. Rapamycin-loaded polysorbate 80-coated PLGA nanoparticles: optimization of formulation variables and in vitro anti-glioma assessment. *J Drug Delivery Sci Technol*. 2019;52:488–499. doi:10.1016/j.jddst.2019.05.026

31. Najm MB, Rawas-Qalaji M, Assar NH, Yahia R, Hosary RE, Ahmed IS. Optimization, characterization and in vivo evaluation of mupirocin nanocrystals for topical administration. *Eur J Pharm Sci*. 2022;176:106251. doi:10.1016/j.ejps.2022.106251

32. Hussain Z, Pandey M, Choudhury H, et al. Hyaluronic acid functionalized nanoparticles for simultaneous delivery of curcumin and resveratrol for management of chronic diabetic wounds: fabrication, characterization, stability and in vitro release kinetics. *J Drug Deliv Sci Technol*. 2020;57:101747. doi:10.1016/j.jddst.2020.101747

33. Hussain Z, Pandey M, Thu HE, et al. Hyaluronic acid functionalization improves dermal targeting of polymeric nanoparticles for management of burn wounds: in vitro, ex vivo and in vivo evaluations. *Biomed Pharmacother*. 2022;150:112992. doi:10.1016/j.biopha.2022.112992

34. Zhuo F, Abourehab MAS, Hussain Z. Hyaluronic acid decorated tacrolimus-loaded nanoparticles: efficient approach to maximize dermal targeting and anti-dermatitis efficacy, Carbohydr. *Polym*. 2018;197:478–489.

35. Eccles S, Aboagye O, Ali S, et al. Critical research gaps and translational priorities for the successful prevention and treatment of breast cancer. *Breast Cancer Res*. 2013;15(5):R92. doi:10.1186/bcr3493

36. Lee HM, Jeong YI, Kim DH, et al. Ursodeoxycholic acid-conjugated chitosan for photodynamic treatment of HuCC-T1 human cholangiocarcinoma cells. *Int J Pharm*. 2013;454(1):74–81. doi:10.1016/j.ijpharm.2013.06.035

37. Madawi EA, Al Jayoush AR, Rawas-Qalaji M, et al. Polymeric nanoparticles as tunable nanocarriers for targeted delivery of drugs to skin tissues for treatment of topical skin diseases. *Pharmaceutics*. 2023;15(2):657. doi:10.3390/pharmaceutics15020657

38. Hussain Z. Nanotechnology guided newer intervention for treatment of osteoporosis: efficient bone regeneration by up-regulation of proliferation, differentiation and mineralization of osteoblasts. *Int J Polym Mater Polym Biomater*. 2019;70(1):1–13. doi:10.1080/00914037.2019.1683558

39. Frigaard J, Jensen JL, Galtung HK, Hiorth M. The potential of chitosan in nanomedicine: an overview of the cytotoxicity of chitosan based nanoparticles. *Front Pharmacol*. 2022;13:880377. doi:10.3389/fphar.2022.880377

40. Pandey M, Choudhury H, Gunasegaran TAP, et al. Hyaluronic acid-modified betamethasone encapsulated polymeric nanoparticles: fabrication, characterisation, in vitro release kinetics, and dermal targeting. *Drug Deliv Transl Res*. 2019;9(2):520–533. doi:10.1007/s13346-018-0480-1

41. Yusuf A, Almotairy ARZ, Henidi H, Alshehri OY, Aldughaim MS. Nanoparticles as drug delivery systems: a review of the implication of nanoparticles' physicochemical properties on responses in biological systems. *Polymers*. 2023;15(7):1596. doi:10.3390/polym15071596

42. Ridolfo R, Tavakoli S, Junnuthula V, Williams DS, Urtti A, van Hest JCM. Exploring the impact of morphology on the properties of biodegradable nanoparticles and their diffusion in complex biological medium. *Biomacromolecules*. 2021;22(1):126–133. doi:10.1021/acs.biomac.0c00726

43. Sharifi-Rad J, Quispe C, Patra JK, et al. Paclitaxel: application in modern oncology and nanomedicine-based cancer therapy. *Oxid Med Cell Longev*. 2021;2021(1):3687700. doi:10.1155/2021/3687700

44. Shafique M, Sohail M, Minhas MU, et al. Biofunctional hydrogel membranes loaded with chitosan nanoparticles for accelerated wound healing. *Int J Biol Macromol*. 2021;170:207–221. doi:10.1016/j.ijbiomac.2020.12.157

45. Chiesa E, Dorati R, Conti B, et al. Hyaluronic acid-decorated chitosan nanoparticles for CD44-targeted delivery of everolimus. *Int J mol Sci*. 2018;19(8):2310. doi:10.3390/ijms19082310

46. Yu T, Li Y, Gu X, Li Q. Development of a hyaluronic acid-based nanocarrier incorporating doxorubicin and cisplatin as a pH-sensitive and CD44-targeted anti-breast cancer drug delivery system. *Front Pharmacol*. 2020;11:532457. doi:10.3389/fphar.2020.532457

47. Kim JH, Kim YS, Kim S, et al. Hydrophobically modified glycol chitosan nanoparticles as carriers for paclitaxel. *J Control Release*. 2006;111(1–2):228–234. doi:10.1016/j.jconrel.2005.12.013

48. Min KH, Park K, Kim YS, et al. Hydrophobically modified glycol chitosan nanoparticles-encapsulated camptothecin enhance the drug stability and tumor targeting in cancer therapy. *J Control Release*. 2008;127(3):208–218. doi:10.1016/j.jconrel.2008.01.013

49. Wang J, Liu D, Guan S, et al. Hyaluronic acid-modified liposomal honokiol nanocarrier: enhance anti-metastasis and antitumor efficacy against breast cancer. *Carbohydr Polym*. 2020;235:115981. doi:10.1016/j.carbpol.2020.115981

50. Negi LM, Jaggi M, Joshi V, Ronodip K, Talegaonkar S. Hyaluronic acid decorated lipid nanocarrier for MDR modulation and CD-44 targeting in colon adenocarcinoma. *Int J Biol Macromol*. 2015;72:569–574. doi:10.1016/j.ijbiomac.2014.09.005